Interference stabilization of complex molecular Fano resonances

A thesis presented for the degree of
M. Sc. in Optical Sciences

Candidate: **Nicola Mayer**

Supervisors: **Misha Ivanov, Oleg Kornilov**

Institut für Physik
Humboldt-Universität zu Berlin
WS17/18

Abstract

Progress in short-pulsed laser technology has opened a route to time-resolved XUV spectroscopy with unprecedented time-resolution of hundreds of attoseconds.
Taking advantage of this development, several recent studies have focused in particular on the dynamics of Fano resonances. First explained theoretically by U. Fano as the result of interference between direct and indirect paths to ionization, these kind of resonances appear ubiquitously in quantum systems.
The simplest case of an isolated autoionizing state coupled to the ionization continuum has been studied extensively both theoretically and experimentally. Yet, more complex examples of Fano dynamics, where more than one state participate in the autoionization process, are still not well understood. For example, the case of two discrete states coupled to a common continuum has been known to lead to the effect of interference stabilization, where one of the states' lifetime increases for increasing coupling strength; however, the effect of interference stabilization on the autoionizing processes in molecules has not been observed until recently.
In 2015, a photoelectron spectroscopy experiment on the window Fano resonance at 17.33 eV in N_2 showed that two Rydberg states, the $(B^2\Sigma_u^+)3d\pi_g$ and $(B^2\Sigma_u^+)4's'\sigma_g$ members of the Hopfield 'emission' series, are at play in the complex autoionizing dynamics. To develop the theoretical description of the N_2 experiment, the interference stabilization effect was included in this thesis in the framework of Fano's theory of autoionization in the time-domain. The general case of two discrete states coupled to an arbitrary number of continua was considered, with the aim of resolving existing discrepancies between theory and experiment on the above-mentioned autoionizing resonance in N_2.
In the **first chapter**, Fano's theory of autoionizing resonances in the energy-domain is discussed. To make direct comparisons with time-resolved experiments and observations, the description of autoionization in the time-domain is also included. Since the necessary parameters to theoretically describe a Fano resonance are usually provided by electronic structure calculations, the electronic structure of molecules, its notation and the theoretical and numerical methods used to calculate it are briefly described. At the end of the chapter, I focus on the case of N_2 and its autoionization series, including the window resonance at 17.33 eV.
In the **second chapter**, two of the most frequently used experimental techniques to record electron dynamics in real time, transient absorption and photoelectron spec-

troscopy, are discussed. The experimental setup and results of the time-, angular- and energy-resolved photoelectron experiment recently performed on N_2 are addressed. In particular, I show how the analysis of the data suggests the presence of the interference stabilization effect at play in the complex electron dynamics that leads to autoionization.
In the **third chapter**, the case of two autoionizing states coupled to an arbitrary number of continua is included in the existing theoretical framework. This generalization leads to novel theoretical results, including the partially balanced and unbalanced case of interference stabilization and the resulting time-dependent populations and photoelectron and absorption spectra.
In the **fourth chapter**, the interference stabilization theory is applied to the case of the Fano resonance at 17.33 eV in N_2. The description of the theoretical model and the resulting theoretical lineshape profiles are shown. The theoretical calculations fit remarkably well with the experimental data and thus prove that the effect can describe the observed autoionization process.

Deutsche Abstrakt

Fortschritte in der Ultrakurzpulslasertechnologie haben den Weg für zeitaufgelöste XUV Spektroskopie mit zuvor unerreichter zeitlicher Auflösung von einigen hunderten Attosekunden erffnet.
Jüngste Studien haben diese Entwicklung insbesondere genutzt um die Dynamiken von Fano-Resonanzen zu erforschen. Diese Art von Resonanzen, die als erstes theoretisch von U. Fano als Ergebnis der Interferenz zwischen direkten und indirekten Pfaden zur Ionisation beschrieben wurden, erscheinen allgegenwärtig in Quantensystemen.
Der einfachste Fall eines isolierten Autoionisationszustands gekoppelt and das Ionisationskontinuum wurde intensiv sowohl in Theorie als auch im Experiment erforscht. Komplexere Beispiele von Fano-Dynamiken, bei denen mehr als ein Zustand im Autoionisationsprozess beteiligt ist, sind jedoch immer noch nicht gut verstanden. So ist zum Beispiel bekannt, dass es im Fall von zwei diskreten Zuständen, die mit einem gemeinsamen Kontinuum interagieren, zum Effekt der Interferenzstabilisation kommen kann, bei der sich die Lebenszeit einer der Zustände mit der Kopplungsstärke vergrößert; jedoch wurde dieser Effekt bis vor kurzem nicht in Molekülen beobachtet. Ein Photoelektronenspektroskopie-Experiment and der Fano-Resonanz von N_2 bei 17.33 eV aus dem Jahr 2015 zeigte, dass zwei Rydberg Zustände, die $(B^2\Sigma_u^+)3d\pi_g$ und $(B^2\Sigma_u^+)4`s'\sigma_g$ Zustände der Hopfield-"Emissions"-Serie, zu der komplexen Autoionisationsdynamik beisteuern. Um eine theoretische Beschreibung des N_2 Experiments zu entwickeln, habe ich in dieser Thesis den Effekt der Interferenzstabilisierung in Fanos Theorie der Autoionisation in der Zeitdomäne aufgenommen. Weiterhin habe ich den generelleren Fall von zwei diskreten Zuständen, die an eine beliebige Anzahl von Kontinua gekoppelt sind, untersucht, um Diskrepanzen zwischen der Theorie und dem Experiment an den erwähnten Autionisationsresonanzen in N_2 zu erklären.
Im **ersten Kapitel** wird Fanos Theorie der Autoionisationsresonanzen in der Energiedomäne besprochen. Um den direkten Vergleich zwischen zeitaufgelösten Experimenten ziehen zu können, wird ebenso die Autoionisation in Zeitdomäne besprochen. Da die nötigen Parameter um Fano-Resonanzen beschreiben zu können üblicherweise von Elektronenstrukturberechnungen stammen, wird die Elektronenstruktur der Moleküle, ihre Notation und die genutzten theoretischen und numerischen Methoden zur Berechnung kurz beschrieben. Am Ende befasse ich mich mit N_2 und seinen Autoionisationsserien, inklusive der Fano-Resonanz bei 17.33 eV.
Im **zweiten Kapitel** werden zwei der am meisten genutzten experimentellen Techniken

um Elektronendynamiken in der Zeitdomäne zu untersuchen beschrieben: Transiente Absorption und Photoelektronenspektroskopie. Besprochen wird weiterhin der experimentelle Aufbau und Ergebnisse des zeit-, winkel- und energieaufgelsten Photoelektronenexperimentes an N_2. Insbesondere zeige ich wie die Analyse der Ergebnisse auf die Existenz von Interferenzstabilisierung in den komplexen Elektronendynamiken, die zur Autoionisation führen, hindeuten.
Im **dritten Kapitel** wird der Fall von zwei Autoionisationszuständen, die an eine beliebige Anzahl von Kontinua gekoppelt sind, in die bestehende Theorie aufgenommen. Diese Generalisierung führt zu neuen Ergebnissen wie dem partiell-ausgeglichenem und unausgeglichenem Fall von Interferenzstabilisierung und den daraus resultierenden zeitabhängigen Populationen sowie Photoelektronen- und Absorptionsspektren.
Im **vierten Kapitel** wird die Theorie der Interferenzstabilisierung auf die Fano-Resonanz von N_2 bei 17.33 eV angewandt. Die Beschreibung des theoretischen Modells und die daraus resultierenden theoretischen Linienprofile werden gezeigt. Die Berechnungen stimmen bemerkenswert gut mit den experimentellen Ergebnissen überein und beweisen, dass der beobachtete Autoionisationsprozess durch Interferenzstabilisierung beschrieben werden kann.

Contents

Introduction

The study of electron dynamics is of fundamental importance to many different fields in physics, from solid state to atomic and molecular physics. Electronic and nuclear motions generally span different timescales due to the large difference in mass of electrons and nuclei (figure 1); vibrations and rotations of nuclei unfold on times ranging from the few femtoseconds to the hundreds of picoseconds, while electrons usually move on the scale of few attoseconds to few femtoseconds. In the energy-domain picture, this corresponds to few tens to hundreds of meV spacing in vibrational and rotational states and to eV separation in electronic ones (figure 1).

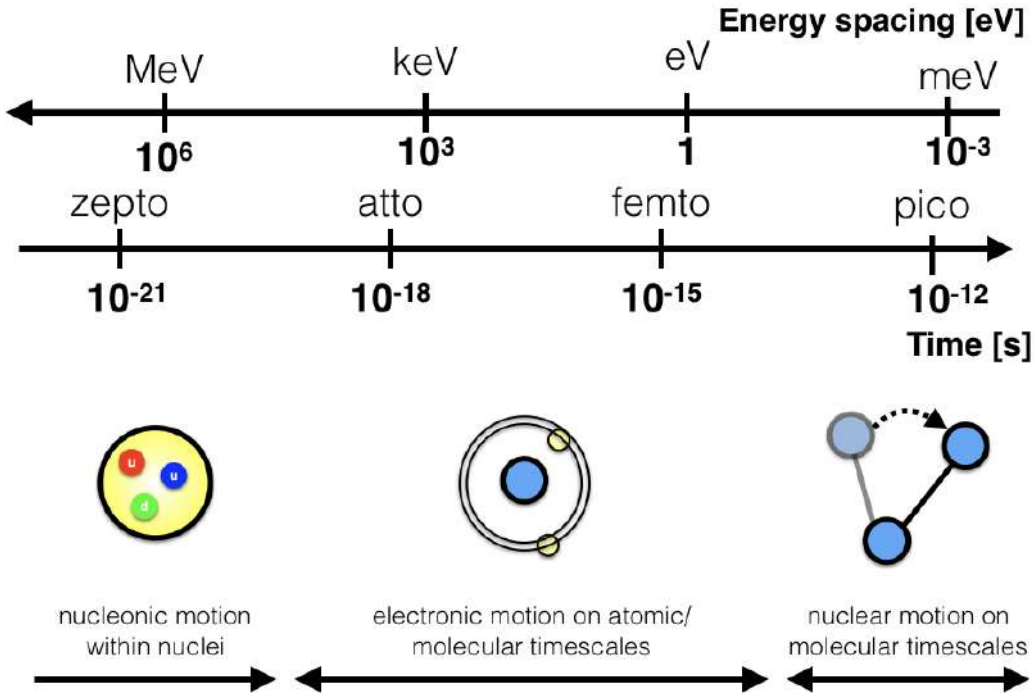

Figure 1: The relevant timescales and corresponding energy spacing between different levels for microscopic motion.

In order to create and probe electronic wavepackets, light sources providing short wavelength from the VIS to the XUV spectrum are therefore needed. Until recently, short pulsed sources in XUV were not available and the dynamics could only be studied indirectly by analyzing the line profiles of electronic resonances in static XUV absorption spectra, the latter usually provided by synchrotron light sources. However, the analysis of the lineshapes can become a difficult task, especially when the profile is the result of complex underlying electronic dynamics. In this case, time-resolved experiments and time-domain approaches can be beneficial.
The observation of the evolution of a spectral feature in time can help disentangle the single electronic contributions to the total signal and, benchmarking the experiment with theoretical predictions, assign contributing electronic states. While femtosecond

techniques are suitable for investigation of *slow* motions such as isomerization in photosensitive molecules, in order to observe an electron moving in real-time we need to use the toolbox of attosecond technology [1]. The recent advances in this field like High Harmonic Generation (HHG) and isolated attosecond pulses [1] provide indeed exceptional time resolution down to the natural timescales on which the electronic dynamics unfolds.

Autoionizing resonances

In this thesis, I will focus in particular on one of the most basic electronic processes: autoionization. In static absorption measurements, autoionization processes lead to absorption lines with characteristic asymmetric shapes. Also called Fano resonances, they owe their name to the italian-american physicist Ugo Fano, who first explained them in 1935 [3] and later described them in a seminal paper in 1961 [2]. Fano resonances occur whenever a discrete state is coupled to a continuous band of states, appearing in the absorption spectrum of quantum systems as an asymmetric lineshape (figure 1.2)

$$\sigma(\epsilon) = \frac{(q+\epsilon)^2}{1+\epsilon^2} \tag{1}$$

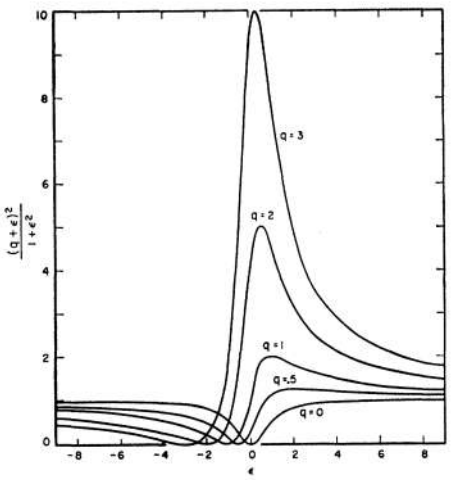

Figure 2: The Fano profile. Figure adapted from [2].

where σ is the normalized absorption cross-section and ϵ the dimensionless energy. Such lineshape is the result of interference between the direct pathway to the continuum state and the indirect one through the discrete state - q being here the famous Fano parameter which depends roughly on the ratio between the probability of transition through the direct and indirect paths. First applied to autoionizing states in helium atoms [2], Fano's theory is used nowadays ubiquitously as it can describe phenomena ranging from Electromagnetically Induced Transparency (EIT) to the Autler-Towns effect [4].
In this thesis I will focus on the Fano resonance in the absorption spectrum of the N_2 molecule at 17.33 eV, which belongs to the $nd\pi_g$ series converging to the $B^2\Sigma_u^+$ state of the ion. Compared to *simple* autoionizing profiles, this window resonance cannot be described in the standard Fano formalism. Specifically, in his 1961 paper Fano considered three cases in the spectral domain: a single discrete state coupled to one continuum, a number of discrete states coupled to one continuum and a single discrete state coupled to a number of continua. This resonance instead is ascribable to the fourth case: two discrete states coupled to a number of continua [5, 6].

The interaction of two states with a common continuum can induce a counter-intuitive but well known effect: the stabilization of a decaying state with increasing coupling strength. The effect is commonly called *interference stabilization* or *interference narrowing* [7–11]. Despite the large body of theoretical work present in the literature, the case of two discrete states coupled to a number of continua was not considered before. However, this is the case needed to describe the realistic situation of the N_2 molecule resonance at 17.33 eV. I will tackle the autoionizing process by using the standard time-dependent formalism introduced by Popov, Movsesian and others, with the goal of including in the existing framework this new case.

The choice of a time-dependent approach to describe autoionizing resonances provides a direct comparison with time-resolved experiments, as the novel available tools in time-resolved science allow us to *film* the evolution of autoionizing resonances on their natural timescales. Control of such resonances via an external light field was also recently shown to be possible [12].

In the first chapter of the thesis, after introducing the main theoretical methods used to calculate the electronic states of a molecular system, I will focus on the spectral- and time-domain description of autoionization. The chapter is concluded by the description of the electronic structure of N_2 and its autoionization features.

In the second chapter, I will introduce the time-resolved experimental techniques used nowadays to study electronic dynamics in atoms and molecules, focusing on photoelectron and transient absorption spectroscopy. Results from a time-, angular- and energy-resolved photoelectron experiment recently performed on the N_2 resonance at 17.33 eV will be discussed at the end of the chapter, together with a brief description of the experimental setup.

The third chapter describes the interference stabilization effect in autoionization, where novel theoretical results stemming from the inclusion of the above-mentioned case of two states coupled to a number of continua in the existing theoretical framework will be described.

Finally, I will show how the inclusion of the interference stabilization effect in the time-dependent Fano picture of autoionization can shed light on multi-electron dynamics, providing a simple qualitative description of the process and - using previous theoretical and experimental data [5,13,14] - solve the existing disagreements between ab-initio calculations and spectroscopical data of the N_2 resonance at 17.33 eV.

Chapter 1

Autoionization in molecules

At the start of this chapter I will focus on autoionization in molecules by describing the process from the point of view of Fano's theory. Such approach will be explained both in energy- and time-resolved fashion, that is through the Stationary and Time-Dependent Schrödinger equation respectively, as it will be necessary later on in the thesis when I will describe the interference stabilization effect.
The necessary parameters for Fano's theory, for example the resonance energy E_r, its width Γ and the Fano parameter q itself, are usually provided by electronic structure calculations. I will therefore discuss the electronic structure of molecules and give a general overview of the theoretical methods used to calculate it.
The Born-Oppenheimer approximation will be first introduced since it constitutes the basic ground on top of which computational methods for calculating electronic states are built. I will then briefly introduce numerical approaches such as Hartree-Fock and Configuration Interaction methods and the notation typically used to indicate the various properties of electronic states in molecules.
In the last part of this chapter, I will focus on the nitrogen molecule N_2, where I applied the theory of interference stabilization to explain previously unresolved discrepancies between theoretical and experimental data. The electronic structure of N_2 and its autoionization features in the region of the XUV spectrum between 17 and 18.9 eV will be briefly described.

1.1 Autoionization

Whenever a molecule absorbs or emits a photon of frequency ω, a transition between two states E_1 and E_2 occurs. Conservation of energy requires that

$$\hbar\omega = |E_1 - E_2| \tag{1.1}$$

In general, we can speak of two kinds of states that can be involved in such a transition: discrete and continuum states. The first are the states with a well defined energy and appear in the spectrum as lines centred around the corresponding frequency $\omega = E/\hbar$.

Continuum states instead appear in the spectrum as broader (ideally flat) lineshapes and span a continuum of energy. This is due to the fact that, while an electron in a discrete state is subject to the parent ion potential and is thus confined to a certain region in space, electrons in continuum states are not bound to the nucleus and they are thus describable as free particles. As a result, their energy is not quantized.
Transitions can therefore occur between any of these states: in a photoionization process for example, an atom or a molecule M absorbs a photon with an energy greater than its ionization potential and emits an electron in the continuum, leaving behind the ion M^+. This corresponds to a transition between a discrete electronic state, the one where the system starts from, and a continuum state where the electron is emitted. The rate of such bound-free transitions can be greatly modified when a discrete state is embedded into the continuum. Such structured continuum states occur naturally in molecular systems when an excited bound state of the neutral molecule lies above the energy of the states of the molecular ion and a coupling between the two is present. In this case, the neutral molecule can absorb a photon and be excited to such a bound state and subsequently decay by emitting an electron and relaxing to the lower ionic state. This process is what we call ***autoionization***:

$$M + \hbar\omega \rightarrow M^* \rightarrow M^+ + e^- \tag{1.2}$$

Due to the mixing between a bound state and a continuum of states, the line profile of an autoionizing state is asymmetrical (see figure 1.1). While these kind of profiles were first observed in the 1930s, the underlying theory explaining their shape was first published only some thirty years later by U. Fano in 1961 [2]. In the next section I will thus go through Fano's theory.

1.1.1 The Fano profile

In his paper from 1961 on autoionization, Fano explains the asymmetrical lineshape as a result of interference between the two possible pathways leading to ionization: the direct ionization from the initial state to the continuum and the indirect path through the autoionizing state (figure 1.1).
To go through Fano's theory of autoionizing resonances, let us consider a system composed of three states: the initial state $|i\rangle$, the autoionizing state $|n\rangle$ and the ionization continuum $|E\rangle$. The Hamiltonian is $\hat{H} = \hat{H}_0 + \hat{V}$, $\hat{H}_0$ being the *field-free* Hamiltonian and $\hat{V}$ the interaction coupling the AIS to the continuum [1]. Fano proceeds to diagonalize the submatrix of the total Hamiltonian describing the interaction between the state $|n\rangle$ and the continuum $|E\rangle$ by looking for an eigenstate of the form

$$|\Psi\rangle = a_n |n\rangle + \int dE' a_{E'} |E'\rangle \tag{1.3}$$

[1] The term $\hat{V}$ has been traditionally called *configuration interaction*, since it describes the interaction between the electronic configurations of the neutral molecule and the ion with one electron in the ionization continuum.

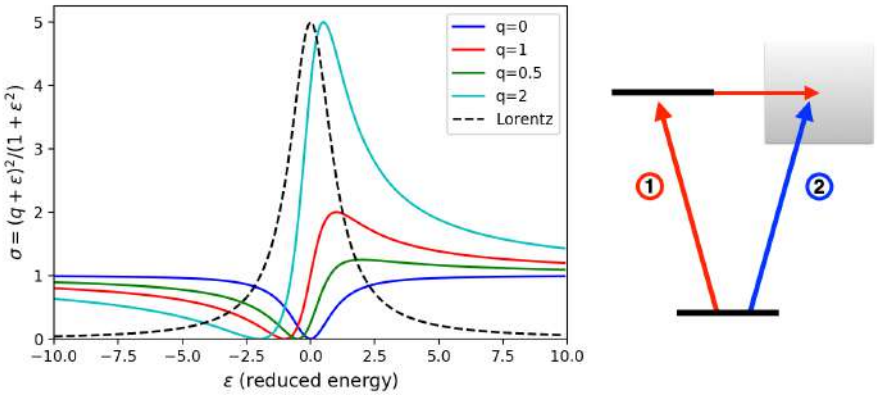

*Figure 1.1: In the left panel, the Fano resonance profile is plotted as a function of the reduced energy $\epsilon = (E - E_n - F(E))/(\Gamma/2)$ for different q values. The black dotted line corresponds to the asymptotic case of a Lorentzian profile ($q \to \infty$). In the right panel, the two possible pathways of ionization are labeled: **1** is the indirect path through the autoionizing states while **2** is the direct path into the ionization continuum.*

which is inserted as an ansatz in the Schrödinger equation $\hat{H}\,|\Psi\rangle = E\,|\Psi\rangle$, yielding a system of coupled equations for the AIS and continuum amplitudes. Without going through the mathematical details, I present his final result:

$$|\Psi\rangle = \frac{1}{\pi V_E^*} \sin\Delta\,|\Phi\rangle - \cos\Delta\,|E\rangle \tag{1.4}$$

where $V_E = \langle n|\,\hat{V}\,|E\rangle$ is the transition element for the bound-continuum transition and $|\Phi\rangle = |n\rangle + P\int dE' \frac{V_{E'}|E\rangle}{E-E'}$ is the state $|n\rangle$ modified by the interaction with the continuum. Δ is the phase shift induced by the interaction, which will be imprinted on the asymptotic behaviour of the continuum plane waves $\sin(\mathbf{k}\cdot\mathbf{r} + \Delta)$ and can be written as

$$\Delta = -\arctan\frac{\pi|V_E|^2}{E - E_n - F(E)} \tag{1.5}$$

where $F(E) = P\int dE' \frac{V_{E'}|E\rangle}{E-E'}$ is the energy shift of the discrete resonance due to its interaction with the continuum. It is clear from the above expression that the phase shift will vary by a factor of π as the energy is scanned across the resonance $E_n + F(E)$. The absorption spectrum can be found by considering the matrix element $\langle g|\,\hat{T}\,|\Psi\rangle$, $\hat{T}$ standing here for a suitable transition operator like the external field coupling the ground state to the bound and continuum states. The modulus square of the matrix element corresponds thus to the total probability of transition from the initial state $|i\rangle$ to the final eigenstate $|\Psi\rangle$ through the two possible paths. The result is the famous *Fano profile*

$$\sigma_{abs} = \frac{(q+\epsilon)^2}{1+\epsilon^2} \tag{1.6}$$

where $\epsilon = \frac{E-E_n-F(E)}{\Gamma/2}$ is the reduced energy, $\Gamma = 2\pi|V_E|^2$ the width of the resonance, and q is the famous Fano parameter

$$q = \frac{\langle\Phi|\,\hat{T}\,|i\rangle}{\pi V_E^*\,\langle E|\,\hat{T}\,|i\rangle} \tag{1.7}$$

which depends on the relative strength between the two pathways of ionization. In an absorption experiment, the Fano parameter is thus completely determined by the internal parameters of the atomic or molecular target. It is clear that as q changes the lineshape will change accordingly (figure 1.1); reflecting the interference between the two paths. In the case of large Fano parameters, a Lorentzian profile is obtained as expected: the only path to ionization is through the resonance. For $q = 0$ instead, a window resonance is obtained and no excitation of the continuum at the resonant energy is possible. For intermediate cases, the destructive interference leads to a zero probability of exciting a state when $\epsilon = -q$ and the profile becomes strongly asymmetrical. In his paper, Fano was able to fit the experimental lineshapes of the autoionizing states of the He atom, a further proof of his correct analysis.
Clearly, Fano's approach is formulated in the energy-domain. Autoionizing resonances typically decay on timescales of few to few tens of femtoseconds and are thus difficult to observe in real-time. However, recent advances in time-domain methods open the possibility of studying the autoionization process as it unfolds on its natural timescales [5, 6, 16, 17]. It is therefore interesting to provide a complementary time-dependent description of the autoionization process, which I will do in the next paragraphs.

1.1.2 Time-dependent description of Fano resonances

In order to treat the process of autoionization in a time-dependent fashion, I will use a semi-classical approach where the molecule is quantized and the laser field is treated classically. I again consider a system composed of three states

$$|\Psi(t)\rangle = c_g(t)\,|g\rangle + c_i(t)\,|i\rangle + \int dE c_E(t)\,|E\rangle \tag{1.8}$$

where now the time-dependent Hamiltonian is given by $\hat{H}(t) = \hat{H}_0 + \hat{V} + \hat{H}_I(t)$, sum of the free Hamiltonian $\hat{H}_0$, the configuration interaction $\hat{V}$ and the interaction Hamiltonian $\hat{H}_I(t) = -\hat{d}\cdot\mathcal{E}(t)$, where $\mathcal{E}(t) = A_{XUV}(t)e^{i\omega_{XUV}t}$ is the electric field of a short XUV laser pulse acting on the ground state at time zero and $\hat{d}$ the dipole operator, $A_{XUV}(t) = F_{XUV}f(t)$ being here the envelope of the laser field. Inserting this ansatz in the Time-Dependent Schrödinger equation (TDSE) $\mathrm{i}\partial_t\,|\Psi(t)\rangle = \hat{H}(t)\,|\Psi(t)\rangle$ we obtain a system of coupled equations for the amplitudes:

$$\mathrm{i}\dot{c}_g(t) = -d_{gi}A_{XUV}(t)c_i(t) - \int dE d_{gE}A_{XUV}(t)c_E(t) \tag{1.9}$$

$$\mathrm{i}\dot{c}_i(t) = (E_i - E_g - \omega_{XUV})c_i(t) - d^*_{gi}A^*_{XUV}(t)c_g(t) + \int dEV_{iE}c_E(t) \tag{1.10}$$

$$\mathrm{i}\dot{c}_E(t) = (E - E_g - \omega_{XUV})c_E(t) - d^*_{gE}A^*_{XUV}(t)c_g(t) + V^*_{iE}c_i(t) \tag{1.11}$$

where ω_{XUV} is the frequency of the laser field and atomic units are used. The continuum amplitudes can be *adiabatically eliminated* by supposing that the continuum states are weakly affected by their interaction with the resonance. This is equivalent to approximating $\dot{c}_E(t) \simeq 0$; the integration over all continuum states of the amplitude $c_E(t)$ retains therefore only the contribution near the resonance, that is proportional to $\mathrm{i}\pi\delta(E - E_g - \omega_{XUV})$. The system of equations can thus be reduced to two coupled equations for the ground and discrete state which take into account their interaction with the continuum; by defining the Fano parameter as previously introduced, the time-dependent dipole moment of the system can be found as [17]

$$d(t) = \langle\Psi(t)|\,\hat{d}\,|\Psi(t)\rangle = e^{-i\omega_{XUV}t}\left[c^*_g(t)d_{gi}c_i(t)(1 - \mathrm{i}/q) + \mathrm{i}\pi|c_g(t)|^2|d_{gE}|^2A^*_{XUV}(t)\right] + c.c \tag{1.12}$$

where $c.c$ denotes the complex conjugate. If the ground state is left mostly unperturbed by the external field then $c_g(t) \simeq 1$ and the bound state amplitude can be expressed as

$$c_i(t) = \mathrm{i}e^{-\frac{\Gamma}{2}t}d^*_{gi}(1 - \mathrm{i}/q)A_{XUV}(t) \tag{1.13}$$

Finally, we can assume the excitation to be short in comparison to the autoionization timescales and set it as $A_{XUV}(t) = F_{XUV}\delta(t)$. We then obtain the final expression for the time-dependent dipole response of the system

$$d(t) = e^{-i\omega_{XUV}t}\left[\mathrm{i}\pi|d_{gE}|^2F_{XUV}\delta(t) + \mathrm{i}|d_{gi}|^2(1 - \mathrm{i}/q)^2F_{XUV}e^{-\frac{\Gamma}{2}t}\right]\Theta(t) \tag{1.14}$$

where $\Theta(t)$ is the Heaviside function accounting for causality and $|F_{XUV}|^2$ is the laser intensity. The physical meaning of such expressions is clear: the first term in the parenthesis accounts for the direct excitation into the continuum at the time of arrival of the ultrashort pulse, while the second one represents the indirect path through the autoionizing resonance, accessed through the transition d_{gi}. The AIS decays with $\tau = 1/\Gamma$, where $\Gamma = 2\pi|V|^2$ is again the width of the resonance. The crucial parameter describing the relative phase of the two pathways it the Fano parameter: as q varies, the phase shift of the response after the initial excitation changes. This phase shift, induced by the mixing of the resonant and continuum states, is reflected in the spectral domain by the asymmetric Fano lineshape, which can be found by considering the absorption spectrum, defined as $\sigma_{abs} \propto \mathrm{Im}[d(\omega)]$ ($d(\omega)$ being the Fourier transform of the dipole response).

As mentioned at the start of the chapter, the necessary parameters for Fano's theory are usually provided by electronic structure calculations. In the next part I will thus briefly introduce these numerical approaches, which are in turn based on the Born-Oppeneheimer approximation. This will help us to introduce the spectroscopic notation of molecular resonances employed in the literature.

1.2 Molecular electronic states

1.2.1 The Born-Oppenheimer approximation

The full description of the electronic structure of a molecule is a difficult task to which no analytical solutions can in general be found. Luckily, while the forces acting on nuclei and electrons are comparable in magnitude, their large difference in mass implies that the position of the nuclei can be considered as fixed in space on the typical timescales of electron dynamics. This approximation is the core of the so-called Born-Oppenheimer approximation, first introduced in 1927 [18].
In order to explain how the approximation works, let us consider a molecule consisting for example of two nuclei with masses M together with a number N of electrons. The Hamiltonian of the molecule can be written as

$$\hat{H}_{mol} = \hat{T}_N + \hat{T}_e + \hat{V} = \hat{T}_N + \hat{H}_e \tag{1.15}$$

where $\hat{T}_N$ is the kinetic energy operator of the nuclei, $\hat{T}_e$ the kinetic energy operator of the electrons and $\hat{V}$ is the total potential energy of the system, consisting of the Coulomb interaction between electrons $\hat{V}_{ee}$, between nuclei $\hat{V}_{NN}$ and between electrons and nuclei $\hat{V}_{Ne}$. $\hat{H}_e = \hat{T}_e + \hat{V}$ is hence called the electronic part of the Hamiltonian. The time-independent Schrödinger equation for the molecule is thus

$$\hat{H}_{mol}\Psi(\mathbf{Q}, \mathbf{q}) = E_{tot}\Psi(\mathbf{Q}, \mathbf{q}) \tag{1.16}$$

where $\mathbf{Q}$ includes all nuclear coordinates (spins and positions of the nuclei) and $\mathbf{q}$ the electronic ones. The Born-Oppenheimer approximation consists of separability of the wavefunction into nuclear and electronic parts:

$$\Psi(\mathbf{Q}, \mathbf{q}) = \Phi(\mathbf{Q})\psi(\mathbf{Q}, \mathbf{q}) \tag{1.17}$$

where $\Phi(\mathbf{Q})$ describes the nuclei and $\psi(\mathbf{Q}, \mathbf{q})$ the electrons. Neglecting the influence of the nuclear motion on the electrons, i.e forgetting about the nuclear kinetic operator $\hat{T}_N$, we solve the Schrödinger equation

$$\hat{H}_e\psi(\mathbf{Q}, \mathbf{q}) = E(Q)\psi(\mathbf{Q}, \mathbf{q}) \tag{1.18}$$

where E(Q) corresponds to the **potential energy surface** (PES) over which the nuclei motion has to be solved and depends only parametrically on $\mathbf{Q}$. Once the latter equation is solved and E(Q) is found, the nuclear motion can then be found by solving

$$(\hat{T}_N + E(Q)\psi(\mathbf{Q}, \mathbf{q}))\Phi(\mathbf{Q}) = E_{tot}\Phi(\mathbf{Q}) \tag{1.19}$$

Hence, in the Born-Oppenheimer approximation, equation 1.18 is solved for different values of the nuclear coordinates Q in order to obtain $E(Q)$, which later plays the role of the potential surface on which the nuclear motion is solved. In figure 1.2 I show an example of a PES of a bound state of a diatomic molecule as a function of the relevant coordinate, here the internuclear axis R.

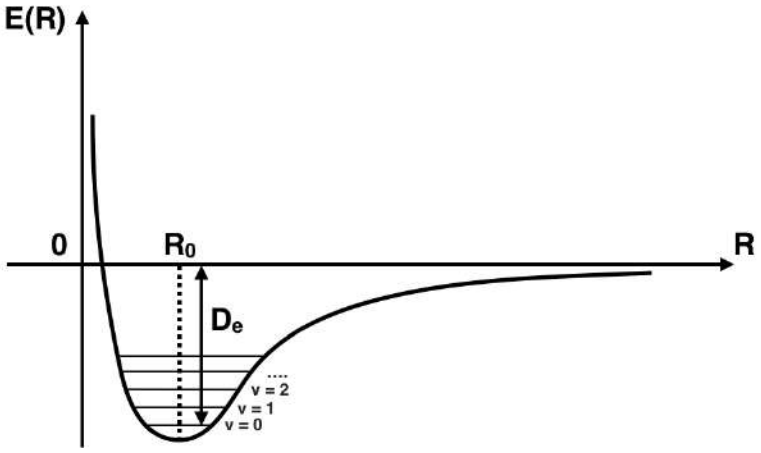

Figure 1.2: The PES of a bound state of a diatomic molecule. As the internuclear distance approaches zero, the repulsion between the nuclei leads to an increase in energy $E(R \to 0) \to \infty$, while for large internuclear distances the potential energy surface approaches asymptotically zero. Around the equilibrium distance R_0, a series of vibrational states are depicted, indicating the possible vibrational states of the nuclear motion $\nu = 0, 1, 2, ...$ D_e stands here for the dissociation energy, the energy required to break the bond between the two nuclei.

1.2.2 Hartree-Fock (HF) and Configuration Interaction (CI) methods

The solution to the electronic equation 1.18 typically requires numerical methods. As it is not the purpose of this work, I will not go into the details of such computational techniques. However, it is important to mention that most of these methods use the Hartree-Fock approximation, which in turn stems from the Born-Oppenheimer and mean-field approximation, as their starting point.
In the mean-field approximation, a single electron moves in the electrostatic potential given by the nuclei and the averaged charge distribution of the remaining electrons. The wavefunction describing the single molecular orbital (MO) ϕ_i is usually built as a linear combination of the atomic orbitals ψ_j (LCAO) of the single nuclei forming the molecule

$$\phi_i = \sum_j c_{ij}\psi_j \tag{1.20}$$

The atomic orbitals ψ_j are in turn expanded on a basis set like Gaussian functions or B-splines and optimized to experimental spectroscopic data.
The MOs are then filled in accordance to the Pauli principle which allows a maximum of two electrons with opposite spins in each orbital. The resulting mean-field is then compared to the initially guessed one and the orbitals' shape is modified accordingly; the Hartree-Fock is therefore a **self-consistent method** where the expansions coefficients c_{ij} are the parameters to optimize, usually via a variational approach with the aim of minimizing the electronic configuration energy. Once the molecular orbitals are

built, the total multi-electron molecular wavefunction has to be anti-symmetric due to the spin-statistics theorem. To enforce this, the total wavefunction is written as a Slater determinant of the MO:

$$|\Psi_e\rangle = \frac{1}{\sqrt{N!}} ||\phi_1\rangle |\phi_2\rangle \dots |\phi_N\rangle| \tag{1.21}$$

Due to the averaging procedure over the charge distribution of the electrons when building the MO, the Hartree-Fock method cannot take in full account the electron-electron correlation. Consequently, there are situations where more sophisticated methods are required in order to reconstruct molecular electronic states.
When several configurations, i.e. different arrangements of electrons in the MOs, are strongly correlated to each other, one of the most frequently used methods is Configuration Interaction (CI). In this approach, the total multi-electron wavefunction is expanded on a set of Slater determinants, the so-called molecular configurations. In its simplest formulation, the molecular configurations consider all possible excitation of single electrons to any virtual orbital. The expansion coefficients on the Slater determinants are then optimized. While the so-called active space of orbitals is limited by computational power, more sophisticated approaches can also include double and triple excitations to virtual orbitals. Physical intuition on the molecular system such as symmetry and physical arguments can further help to obtain a better solution to the problem.

1.2.3 Molecular orbitals notation

As mentioned above, MOs are built starting from atomic orbitals. For a diatomic molecule, at large internuclear distances the MO reduce thus to the single separated atomic orbitals localized on the individual nuclei. As the nuclei are moved closer to each other, linear combinations of the atomic orbitals are taken to form the MOs.
In comparison to atoms, the molecular wavefunctions do not posses spherical symmetry. In the case of a diatomic molecule though, the system is invariant with respect to rotations around the internuclear axis. This implies that the projection of the total angular momentum on the internuclear axis is a conserved quantity to which we can associate a quantum number to classify the electronic states. The term symbol for MOs is the following

$$n\lambda_{g/u} \tag{1.22}$$

where n is the principal quantum number and λ is the projection of the total angular momentum on the internuclear axis. The allowed values for $\lambda = 0, 1, 2, ..$ are labeled respectively with small Greek letters $\sigma, \pi, \delta, ...$ The g/u subscript refers to the inversion symmetry around the center of the molecule. In the case of diatomic molecules, this additional symmetry exists only if the molecule is homonuclear. Depending on the symmetry of the electronic wavefunction, we speak of *gerade*/*ungerade* (g/u) states:

$$\Psi(\mathbf{r}) = \Psi(-\mathbf{r}) \quad \text{gerade} \tag{1.23}$$

$$\Psi(\mathbf{r}) = -\Psi(-\mathbf{r}) \quad \text{ungerade} \tag{1.24}$$

The full molecular wavefunction is then built from combinations of the single MOs, reflecting their symmetry. Here as well we associate a term symbol for the multi-electron wavefunction

$$^{2S+1}\Lambda^{+/-}_{g/u} \tag{1.25}$$

where g/u refers again to the inversion symmetry around the origin of the coordinate system, $2S+1$ is the multiplicity related to the the total spin S of the electrons and Λ is again the projection of the total angular momentum on the internuclear axis. In order to clearly separate it from the term symbol for the single MOs, the allowed values $\Lambda = 0, 1, 2, ..$ are associated with capital greek letters $\Sigma, \Pi, \Delta, ..$. $+/-$ refers instead to the additional symmetry for these states with respect to reflection in an arbitrary plane containing the internuclear axis.
Now that I have introduced the main approximations in calculating the electronic structure of molecular systems and the notation used in spectroscopy to classify the different states, I can focus on a particular kind of electronic states that are found in both atoms and molecules: autoionizing states. These are the kind of states on which I will focus in this thesis work.

1.3 Electronic structure and autoionization of N_2

Nitrogen is mostly found in its molecular form as N_2. It is an example of a homonuclear diatomic molecule, one of the lightest in nature.
While 78% of the total volume of the atmosphere on planet Earth is occupied by N_2 in its gas phase, it is also found ubiquitously in living organisms and is thus one of the main building blocks of our planet's ecosystem [19].
A total of 14 electrons occupy the orbitals of the two N nuclei. 6 of the 10 valence electrons of N_2 participate in its triple bond, which is one of the strongest in nature with a dissociation energy of 9.79 eV [20]. The strong bond can be broken by XUV light: N_2 dissociation from Sun light is for example an important process on Titan, where 98% of the upper atmosphere is composed of nitrogen [21].
Nitrogen plays therefore a crucial role in many environments and the study of its electronic structure can shed light on a number of important processes in nature. In the next two sections, I will give a brief overview of the electronic structure of the ground state of the molecule and focus on the autoionization dynamics of N_2.

1.3.1 The ground state of N_2

Hartree-Fock computations [22,23] show that the ground state wavefunction has a $^1\Sigma^+_g$ symmetry. The occupation of the molecular orbitals is

$$1\sigma_g^2 1\sigma_u^2 2\sigma_g^2 2\sigma_u^2 1\pi_u^4 3\sigma_g^2 \tag{1.26}$$

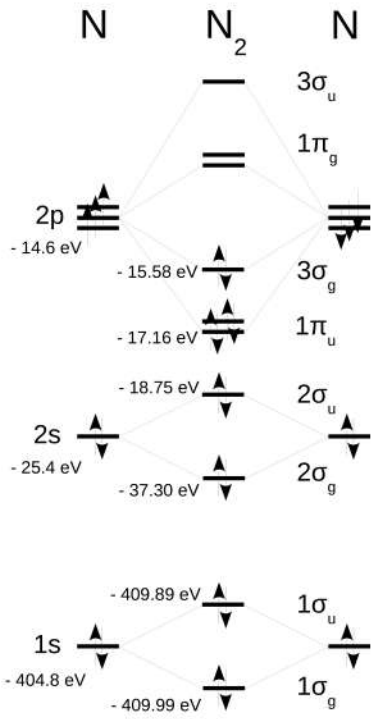

Figure 1.3: Electronic occupation of molecular orbitals in N_2. Image adapted from [22].

Note that the energy ordering of the electronic states strongly depends on the distance between the two ionic cores. The latter configuration is given for its equilibrium distance $R_0 = 1.12$ Å.

1.3.2 Potential energy curves of N_2^+

The potential energy curves for the N_2^+ ion are depicted in figure 1.4. The curves are taken from [22, 24].
In this work only the first three ionic states are going to be considered. The ground and the first excited state, labeled as X and A, of N_2^+ correspond to the removal of an electron from the two outermost molecular orbitals, the $3\sigma_g$ and $1\pi_u$ respectively. The

Term	I [eV]	Configuration
$X^2\Sigma_g^+$	15.5	$3\sigma_g^{-1}$
$A^2\Pi_u^+$	16.9	$1\pi_u^{-1}$
$B^2\Sigma_u^+$	18.9	$2\sigma_u^{-1}$

Table 1.1: Molecular term, ionization thresholds (I) at the equilibrium distance $R_0 = 1.12$ Å and dominant electronic configuration for the first three ionic states of N_2^+. Taken from [22, 24].

second excited state B of the N_2^+ ion corresponds to the removal of an electron from the $2\sigma_u$ orbital. The ionization thresholds at the equilibrium distance R_0, the electronic configuration and the molecular term of the ionic states is reported in table 1.1. Note that, due to the strong correlation between them, the reported configurations are the dominant ones in the numerical calculations.

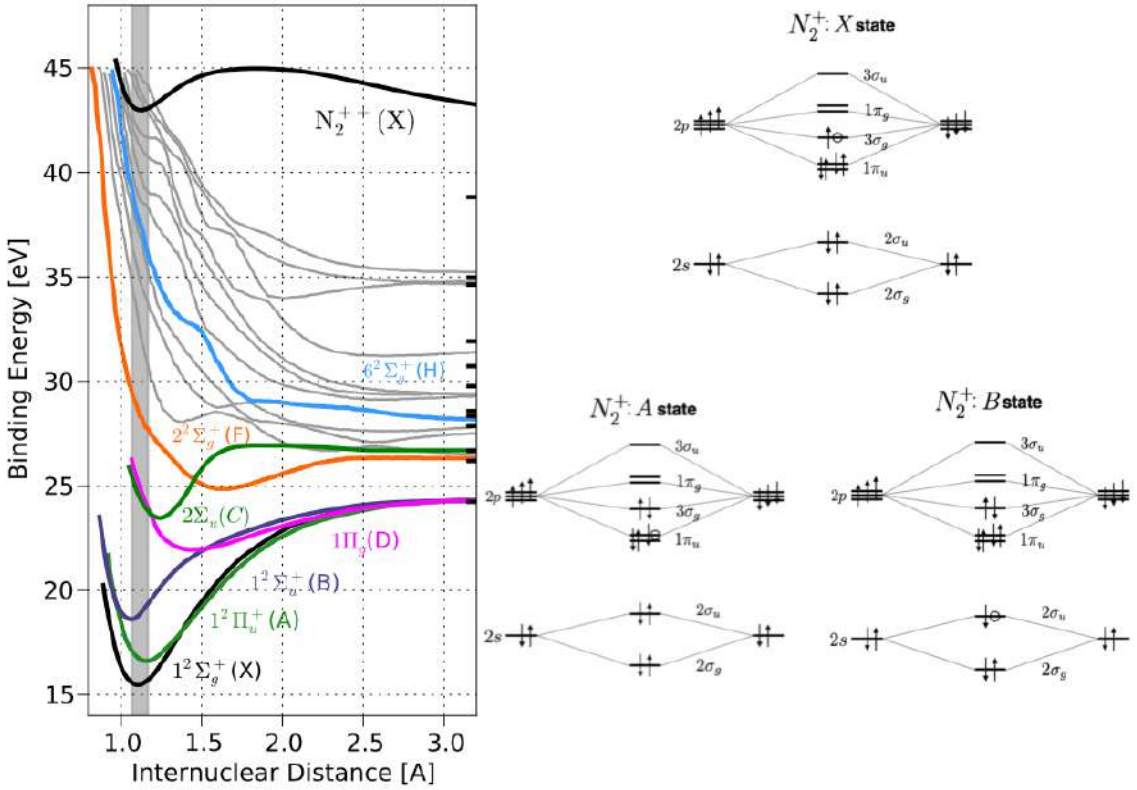

Figure 1.4: Left: potential energy curves as a function of the internuclear distance in N_2^+. Image adapted from [21, 22]. Right: the dominant electronic configuration for the ionic states X, A and B of N_2^+ at $R_0 = 1.14$ Å.

1.3.3 Autoionization in N_2

Autoionizing resonances in N_2 were first studied by Hopfield in 1936 [25], who observed two series of spectral lines converging to a common ionization threshold (figure 1.5). These two series, which Hopfield named the *absorption* and "*emission*" series, correspond to the absorption of an XUV photon leading to excitation of an electron from the $X^1\Sigma_g^+$ ground state of N_2 to highly excited Rydberg states converging to the $B^2\Sigma_u^+$ ionic core, which then autoionize.
The most complete *ab initio* calculations to date from Raoult et al. [13] assign the absorption series to excitation of the Rydberg series $(B^2\Sigma_u^+)n`d'\sigma_g$, where the quotes

indicate d as the dominant component of the orbitals resulting from significant mixing of $nd\sigma$ with $(n+1)s\sigma$ states. This series appears as absorption peaks with slightly asymmetric profiles, corresponding to high values of the Fano parameter q. The emission series resonances exhibit instead a dip in the absorption cross section and are called *window* resonances, corresponding to low q values.
Although high quality spectroscopical data in the XUV region from 17.0 eV to 18.9 eV were recorded as recently as 2011 [26] and *ab initio* calculations suggest that the *emission* series is a result of two Rydberg series overlapping, the $nd\pi_g$ and $(n+1)'s'\sigma_g$, the assignment of the features remains non-trivial as the calculated profiles do not match exactly the recorded experimental data [13]. Specifically, the complex lineshape of the window resonances cannot be fit by a simple Fano profile but rather stems from the superposition of the two contributing states. Furthermore, rotational structure suggesting coupling of rotational degrees of freedom between the $nd\pi_g$ and $(n+1)'s'\sigma_g$ states was observed by Huber et al. in 1993 [27] and such coupling was not included by Raoult et al.

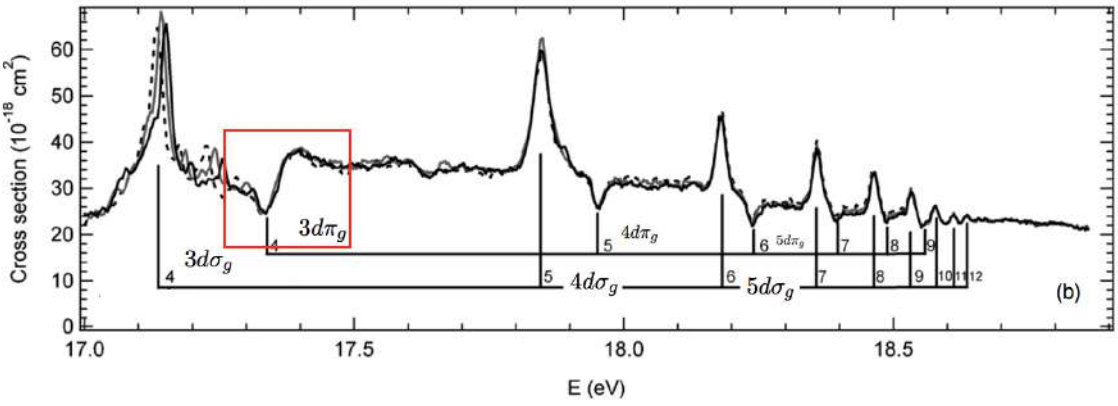

Figure 1.5: Synchrotron absoprtion spectrum of N_2 in the XUV region 17.0-18.9 eV with the line assignments. Highlighted in the red box is the Fano resonance at 17.33 eV investigated in [5]. Image adapted from [26].

Although synchrotron experiments can resolve very fine structures in the absorption and photoelectron spectrum of molecules, in the case of complex line profiles a complementary approach is needed. For example in the case of the window resonances in the XUV region of N_2 where two Rydberg series seem to overlap, a time-domain approach can identify the individual contributions to the total profiles, providing further insight into the electronic dynamics. Recently, a time-, angular- and energy-resolved photoelectron spectroscopy experiment was performed on the Fano resonance at 17.33 eV of N_2 with the aim of disentangling the complex dynamics from which the window profiles arise [5]. In the next chapter, I will therefore first introduce the basic concepts of time-resolved techniques to then discuss in detail the results obtained from this experiment.

Chapter 2

Time-resolved dynamics of autoionizing states

The most widely used configuration for time-domain experiments to study molecular dynamics is a pump-probe setup employing femtosecond pulsed lasers.
I will introduce the pump-probe method in the first section of this chapter, focusing on its basic concepts. Two of the most important time-resolved techniques, transient absorption and photoelectron spectroscopy [1], will be then discussed. I will give an intuitive picture of their theoretical concepts and experimental implementation, with a focus on the definition of the observables that are detected in such experiments.
In the second and last part of this next chapter I will discuss the results of a recently performed time-resolved photoelectron experiment on the Fano resonance at 17.33 eV in N_2 [5], where two electronic states participate in the complex dynamics. The results suggest that the interference stabilization is playing a role.

2.1 Pump-probe techniques

2.1.1 The pump-probe method

In a pump-probe experiment, two short laser pulses are sent on the atomic or molecular sample with a certain temporal delay τ with respect to each other. The first pulse - the pump - triggers the dynamics by exciting the system and *starting the clock*; after some time τ, the second pulse - the probe - *stops the clock* by taking a snapshot of the system's dynamics, projecting them onto a certain final state. As a result, by scanning the temporal delay, we can add together all the recorded snapshots to form a *movie* of the phenomena on its natural timescale. The difference between time-resolved photoelectron and transient absorption spectroscopy (TRPES and TAS respectively) is the kind of snapshots that are taken: in TRPES, the movie is put together by looking

[1] Note that photoelectron spectroscopy requires XUV wavelengths as sufficient photon energies have to be used to ionize molecules.

at the ejected electrons from the ionized sample, while in TAS the spectrum of the probe field after the sample is detected.
In figure 2.1 I depict a typical pump-probe experiment in the form of a common table-top setup in an ultrafast laser laboratory. A short laser pulse is split in two beams - the *pump* beam and the *probe* beam - by means of a beam splitter (**BS**) and sent through two different optical paths. Along one of the paths, two mirrors $\mathbf{M}_3$ and $\mathbf{M}_4$ are mounted on a motorized stage and used to control the difference in the optical path ΔL of the probe beam with respect to the pump. The arrival of the probe beam on the sample is thus delayed by a time $\tau = \Delta L/c$. Finally, a detector **D** records a signal as a function of the scanned delay $S(\tau)$, which contains the features of the dynamic process we seek to investigate in real time. In figure ideal detectors are depicted: in a TAS experiment, the detector collects the light after the sample, i.e. the absorption spectrum; in a PES experiment, the detector collects the electrons and measures kinetic energy and emission angles.
It is instructive to give a more intuitive description of a pump-probe experiment - a wavepacket point of view. Time resolved techniques such as photoelectron spectroscopy and transient absorption spectroscopy rely on the creation and detection of wavepackets on the excited potential energy surfaces of the system under study (see figure 2.1). The typical pump-probe experiment can then, from this point of view, be separated in three main steps [28]: **i**) the creation of a coherent superposition of excited molecular or atomic eigenstates by the pump pulse, i.e. the wavepacket; **ii)** the free evolution of the wavepacket along the potential surfaces of the system; **iii)** the projection of the wavepacket on the target state $|\Psi_n\rangle$ - effectively the screen on which we project the *microscopic movie*.
In the next sections I will introduce two of the most frequently used pump-probe techniques: transient absorption and time-resolved photoelectron spectroscopy. Both techniques have their advantages as well as disadvantages; I will therefore introduce the reader to their basic principles and try to give some guiding lines on how and when to use these powerful tools in order to best observe the different properties of the system under study.

2.1.2 Transient absorption spectroscopy

Transient absorption spectroscopy (TAS) relies on recording spectrally-resolved absorption of atoms, molecules or solids in their excited states. The excited states, prepared by a pump pulse at time t_0, evolve until the probe pulse arrives and makes a snapshot of the absorption spectrum at time $t_0 + \tau$.
While the temporal resolution of a transient absorption setup is given by the control of the delay τ and the coherence between the two fields, the spectral resolution is determined by the characteristic spectral features of the system itself [29]. It is important to note that since time is observed indirectly via the delay τ, transient absorption spectroscopy allows for simultaneous recording of fast dynamics and narrow spectral features without any violation of the time-energy uncertainty [29]. Hence, a transient

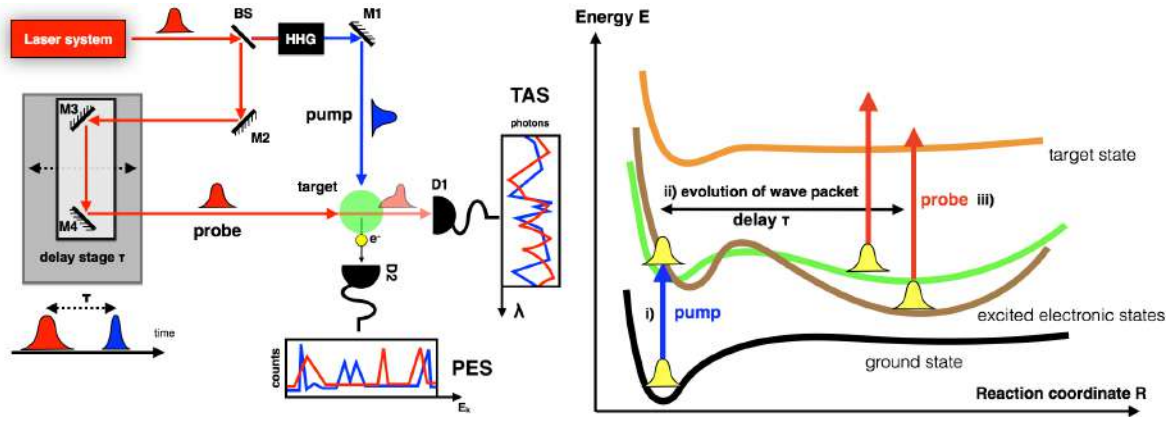

Figure 2.1: ***Left****: a typical pump-probe setup is depicted. Mirrors are denoted by the letters* ***M****, the detectors by* ***D****, beam-splitters by* ***BS****, High-Harmonic Generation by* ***HHG****. The two detection schemes, the TAS and PES, detect respectively the spectrum of the probe pulse and the photoelectrons and record difference signals when the sample is excited (red lines) or not (blue lines). On the bottom left, the sequence of pump and probe pulses.* ***Right****: a wavepacket point of view of a pump-probe experiment is depicted. i) Pump pulse creates a wavepacket. ii) Evolution of the wavepacket according to the TDSE. iii) Probing of the wavepacket by projection on a final target state by the probe.*

absorption measurement can provide high-resolution data both in the spectral and time domain.
Experimentally, one measures the intensity of the incident and transmitted light, respectively $I_0(\lambda)$ and $I(\lambda)$. The absorbance $A(\lambda)$ of each probe pulse is then defined by the Beer-Lambert law

$$A(\lambda) = \log \frac{I_0(\lambda)}{I(\lambda)} \tag{2.1}$$

The change in absorbance induced by the pump pulse can then be expressed as

$$\Delta A(\lambda) = A_p(\lambda) - A_u(\lambda) = \log \frac{I_u(\lambda)}{I_p(\lambda)} \tag{2.2}$$

where the indexes p and u refer to the pumped and unpumped sample.
From a theoretical point of view, the absorption probability per unit frequency at a given frequency and delay τ between the pulses can be expressed as [29]:

$$S(\omega, \tau) = 2\,\mathrm{Im}\left[\tilde{d}(\omega, \tau)\tilde{\mathcal{E}}^*(\omega, \tau)\right] \omega > 0 \tag{2.3}$$

where $\tilde{d}(\omega)$ is the Fourier transform of the dipole response function of the atom or molecule and $\tilde{\mathcal{E}}(\omega, \tau)$ is the two-color field. It is clear that positive or negative $\omega S(\omega)$ correspond to gained or lost energy per unit frequency by the irradiated sample. We can also define a generalized cross-section

$$\tilde{\sigma}(\omega) = g\,4\pi\,\alpha\,\omega \mathrm{Im}\left[\frac{\tilde{d}(\omega)}{\tilde{\mathcal{E}}(\omega)}\right] \tag{2.4}$$

where g is the number of active electrons and $\alpha = 1/c$. Both quantities, the cross-section $\tilde{\sigma}(\omega)$ and the response function $S(\omega)$, are linked to the imaginary part of the dipole spectrum - the dissipative part of the spectral response of the system - which is a quantity that is therefore necessary to simulate theoretically in a TAS experiment.
Due to its many advantages and its relatively easy setup, TAS has been mastered and used over the years to study fast, nuclei-initiated processes like molecular vibrations. Still, the technique has been largely blind to electron dynamics until recently, as researches struggled to find a suitable light pulse to track transient electronic signals on the hundreds attoseconds to few femtoseconds timescale. The advent of High Harmonic Generation (HHG) and attosecond pulses provides a broadband, coherent and short pulsed light source that has become available to many laboratories over the past decade and a half.
Since attosecond pulses are produced by the non-linear interaction of an IR few-cycle field with a noble gas such as Kr [30], they can be precisely synchronized to the oscillations of the carrying IR field. Therefore, using the attosecond XUV pulse together with a clone of the IR field, one can perform two-color attosecond transient absorption (ATAS) experiments on the target system that can be pumped and probed by either field, although the low conversion efficiency of HHG makes it difficult to realize the *ideal experiment* where two XUV pulses serve as pump and probe.
In its first application to study autoionizing resonances, Z. Chang et al. used ATAS to resolve in time the autoionization of the $3s3p^6np\,^1P$ series in Ar [16]. By scanning the delay between a short 130 as XUV pulse and a longer 23 fs NIR pulse, they were able to show control over the peak, linewidth and shape of the Fano resonances by modifying the dipole response with the latter one after excitation by XUV. Moreover recent theoretical results, confirmed experimentally by ATAS, showed that the IR field induces a phase shift which effectively changes the profile of an auto-ionizing resonance from a Fano one to a Lorentzian [12].

2.1.3 Photoelectron spectroscopy

The principle underlying photoelectron spectroscopy (**PES**) is the famous photoelectric effect explained by Einstein in his annus mirabilis [31]: a light source with sufficient photon energy $\hbar\omega$ ionizes an atom or a molecule and the kinetic energy of the ejected electrons is measured by a detector. If the electron was initially in a state with binding energy E_i, conservation of energy requires the kinetic momentum of the electron in the continuum to be

$$E_{kin} = \hbar\omega - E_i \geq 0 \tag{2.5}$$

By measuring the kinetic energies of the outgoing electrons, we can therefore determine the binding energy of the orbital from which they were ejected [15].
In a pump-probe experiment, the pump pulse creates a wavepacket which evolves for a time τ:

$$|\Psi(\tau)\rangle = \sum_i a_i e^{-i\omega_i \tau} |\psi_i\rangle \tag{2.6}$$

The probe pulse $\mathcal{E}_p$ then interacts with the wavepacket and projects it onto a certain final state $|\Psi_f\rangle$. The signal one measures is then given by

$$S(\tau) = \left| \langle \Psi_f | \, \hat{d} \cdot \mathcal{E}_p \, | \Psi(\tau) \rangle \right|^2 \tag{2.7}$$

Choosing this final state $|\Psi_f\rangle$ as an ionization continuum as in PES has its advantages, including the fact that the detection of charged particles is highly sensitive and that the final state in an ionization process is often a stable cation or neutral species which makes the *screen* on which we project our wavepacket a good template for the microscopic movie [28].
Moreoever, by detecting the kinetic energies together with the emission angles of the photoelectrons one can retrieve informations on the shape of the orbitals. Both observables, the kinetic energies and the emission angles of the electrons, can be detected using a Velocity Map Imaging (VMI) spectrometer [32].
A typical VMI setup and its principles are depicted in figure 2.2. Using a VMI it is possible to reconstruct the 3D velocity map distribution of the emitted charges (ions or electrons) by using electrostatic lenses which accelerate the particles toward a micro-channel plate, effectively projecting their velocity distribution onto a 2D plane. Particles with same perpendicular components of their velocity with respect to the normal axis to the 2D detector will end on the same spot on the detector. The detector then sees the integrated distribution along the axis normal to the plane of the 2D detector $\hat{z}$:

$$F(x, y) = \int_{-\infty}^{\infty} f(r, y) dz \tag{2.8}$$

Using $r^2 = x^2 + y^2$ one then obtains the following expression for the 2D projection

$$F(x, y) = 2 \int_{|x|}^{\infty} \frac{f(r, y) r}{\sqrt{r^2 - x^2}} dr \tag{2.9}$$

This is the so-called Abel transform of a 3D distribution. In order to obtain the original distribution, we thus have to find the inverse Abel transform. A variety of computational methods have been designed over the years to solve this problem but, as a common feature, they all rely on enforcing a cylindrically symmetry on the distribution of the particles' velocities. This is usually done by *marking* one spatial direction by choosing a laser with a polarization parallel to the detector screen.
From a theory standpoint, while the energy of the emitted electron is determined by conservation of energy, its angular distribution is found by expanding its wavefunction in the basis of spherical harmonics, the so-called partial waves. Superposition of different partial waves will in turn result in different resulting interference patterns in the angular-resolved photoelectron spectrum. Analyzing the latter together with the knowledge of the available transitions determined by the selection rules, one can therefore reconstruct the symmetry of the molecular or atomic orbital from which the electrons were ejected.

It is clear that by combining the angular- and energy-resolution provided by the VMI with the time-resolution of a pump-probe technique, where differential images of the electrons' momentum distribution are recorded as a function of the delay between pump and probe pulse, we can retrieve very detailed information on the dynamics in the molecular target under study.
This kind of time-, angular- and energy-resolved experiment was recently performed on the Fano resonance of N_2 at 17.33 eV with the aim of identifying and imaging the transient Fano dynamics arising from the two involved electronic states [5]. In the next part of this chapter I will thus go through this experiment and its results as it will become our starting point for the application of the theory of interference stabilization to autoionizing states in molecules.

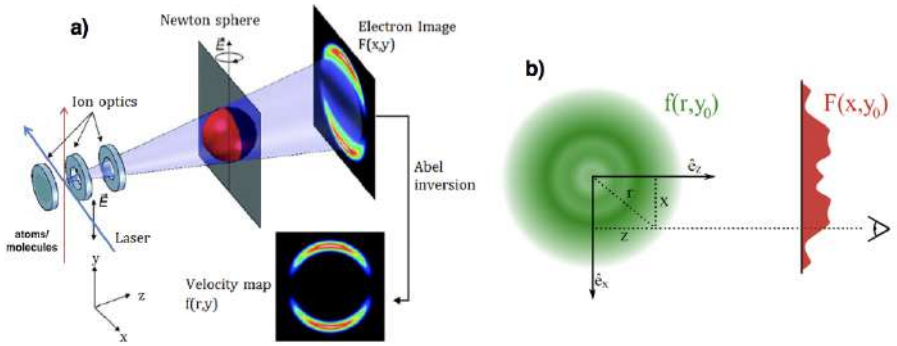

Figure 2.2: Panel ***a)****: setup of a VMI. A laser ionizes the sample and the charged particles are accelerated by the concentric lenses toward the detector. While traveling due to their kinetic energies they expand in the Newton sphere, which is then projected on the detector screen. Panel* ***b)****: the initial distribution $f(r, y)$ and its Abel transform $F(x, y)$. All images are adapted from [33].*

2.2 Time-, angular- and energy-resolved photoelectron spectroscopy of a Fano resonance in N_2

In their paper from 2016 [5], a group of researchers from Berlin and Milan studied the Fano resonance of N_2 at 17.33 eV (figure 2.3) via time-, angular- and energy-resolved photoelectron spectroscopy. As mentioned in the previous chapter, *ab initio* calculations predict two electronic states contributing in this spectral region: the $3d\pi_g$ and the $4's'\sigma_g$ attached to the $B^2\Sigma_u^+$ ion core. The angular-resolution provided by the VMI spectrometer together with the time-resolution of a pump-probe method helped to disentangle their contributions to the detected signal. For two resonances of different symmetry one expects to observe a time-dependent dynamics in the angles of emission of the electrons.
In this section, I first introduce briefly the experimental setup designed to study the

Fano resonance of N_2 and later on discuss the results which, as I will show later, indicate the presence of the interference stabilization effect.
The setup is depicted in figure 2.3. A time-delay compensating monochromator beamline was used to spectrally filter XUV radiation generated in a HHG cell filled with argon gas. By adjusting the parameters of the two diffraction gratings, the monochromator can tune the XUV radiation wavelength by selecting the harmonic order [34]. It was thus possible to produce an XUV pulse centred at 17.5 eV and a FWHM of 0.5 eV, covering therefore the energy range of the spectrum of N_2 where the $3d\pi_g$ member of the Hopfield emission is located. While the XUV radiation populates the excited electronic states, their dynamics is probed by a second IR pulse centred at 795 nm with a 90-nm bandwidth and duration of 20 fs which ionizes the states before they undergo autoionization. The emitted electrons are then recorded by a VMI which allows for the reconstruction of their 3D momentum distribution via a BASEX Abel inversion algorithm [35].
The experimental results are shown in the following figures 2.4, 2.5. On the left of figure 2.4, a slice through the 3D photoelectron momentum distribution is shown. The image is the result of the subtraction between XUV-only and XUV+IR images and is plotted as a false color plot. Red color corresponds to an increase of the signal when the IR is present while blue indicates depletion. The ring labeled X_0 corresponds to the photoelectrons emerging in the $X^2\Sigma_g^+(\nu = 0)$ continuum channel of N_2^+, where ν is the vibrational state of the ionic core. The X_0 channel corresponds thus to the lowest vibrational level of the ground state of N_2^+. Due to the small displacement between the neutral and ionic X potential energy surface, no other vibrational progressions of the electronic state are observed. The outermost ring, labeled X_0+IR, corresponds to the sideband obtained by adding one IR photon to the electron in the X_0 channel. The $A_{0,1}$ rings correspond to the $A^2\Pi_u(\nu = 0, 1)$ continuum channels of the next ionic state; here the vibrational channels are instead active as the potential energy surface is slightly shifted with respect to the ground state of N_2. The corresponding sideband features overlap with the X_0 channel and are thus not visible. Finally, the Ry+IR feature corresponds to the IR-assisted ionization of the excited $3d\pi_g + 4`s'\sigma_g$ state; the researchers thus concluded that the IR pulse is able to ionize the electronic states before autoionization takes place.
The time-dependent signals are shown in the panel **b)** of figure 2.4 as a function of the kinetic energy of the photoelectrons. Time zero here corresponds to the pump and probe pulses arriving at the same time on the sample. While the $A_{0,1}$ and X_0 features are symmetric with respect to time zero, the Ry+IR feature extends toward positive delays. This is expected for an electronic state with a certain lifetime and is therefore a further proof that this feature corresponds to the autoionizing state.
In order to investigate the dynamics of the autoionizing feature, the angular-resolution of the VMI detection is exploited. In the case of ionization by two photons with linear polarizations, the XUV and the IR in this case, the angular distributions from unaligned molecules can be described by two asymmetry parameters $\beta_{2,4}$, which take into account

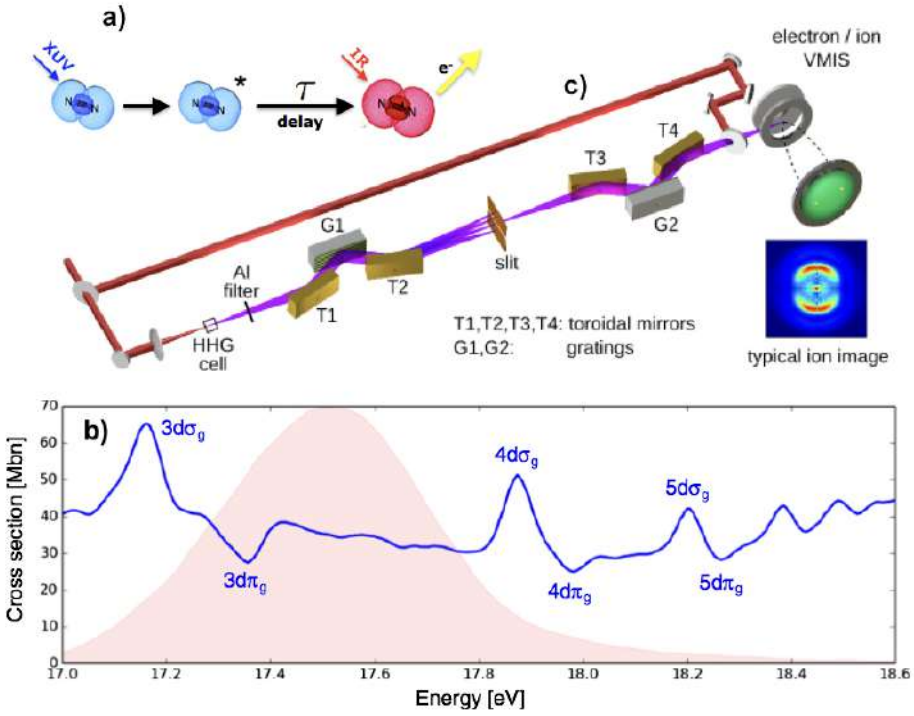

Figure 2.3: Panel ***a)****: the HHG generated and spectrally filtered XUV radiation excites the N_2 molecule which, after a delay τ, is ionized by the IR pulse. Panel* ***b)****: the absorption spectrum of N_2 is shown in blue with the corresponding labeled members of the absorption and emission series. The pink shaded region depicts the spectrum of the XUV radiation used in the experiment. Panel* ***c)****: the beamline. The XUV radiation is filtered by the monochromator, where the positions and angles of the diffraction grating with respect to the axis of propagation of the light are adjusted, to select the harmonics generated in the HHG chamber. The IR radiation co-propagates along the beamline and together with the XUV is focused in the interaction region on the sample. The resulting photoelectrons are then recorded by a VMI spectrometer. All pictures are adapted from [5, 6, 21].*

the weight of different spherical harmonics in the photoelectron wavefunction [5]:

$$\sigma(\theta, E) = \frac{\sigma_0(E)}{4\pi} \left[1 + \beta_2(E) P_2(\cos\theta) + \beta_4(E) P_4(\cos\theta)\right] \tag{2.10}$$

where $\sigma(\theta, E)$ is the doubly differential cross section, $\sigma_0(E)$ the cross-section integrated over all angles, $P_{2,4}$ are the Legendre polynomials and finally E and θ are the energy and polar angles (with respect to the polarization axis) of the photoelectrons. The asymmetry parameters of the Ry+IR feature are plotted in the bottom right of figure 2.5. When β_2 increases, angular distributions are peaked along the polarization axis. The time dependence of the asymmetry parameters is another strong hint at dynamics arising from more than one electronic state, as one single state should not change its emission angles over the scanned delay.

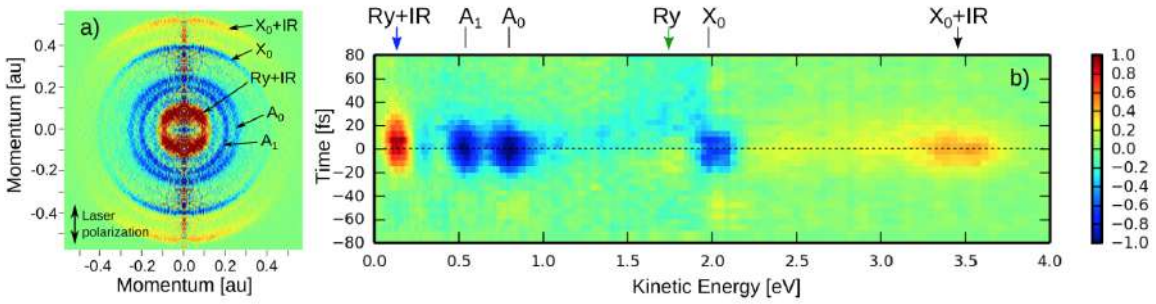

Figure 2.4: Image ***a)****: a slice through the 3D momentum distribution of the photoelectrons. Image* ***b)****: the time-dependent signal integrated over all angles of the labeled features corresponding to the left plot. The x-axis is the kinetic energy of the photoelectrons and thus corresponds to the length of the ray drawn from the center of the 2D projection of the distribution. All figures are taken from [5, 6].*

In order to gain further insight and confirm this hypothesis, the angular distributions of the feature integrated between 0.1 and 0.3 eV were plotted as a function of time in panels **a)** and **b)** of figure 2.5. In order to remove any effect coming from the time-dependent signal intensity, a singular value decomposition (SVD) was performed [36]. This procedure helps removing additional noise (as shown in the plots) and reveals the main components of the total signal as a function of time. It is clear that at time zero the angular distribution is rather uniform while for positive delays the signal peaks at 0° and 180°. The two principal components to the signal are then plotted in panel **c)** of figure 2.5. Their associated decay was then fitted to an exponential decay convoluted with a Gaussian cross-correlation function, yielding lifetimes of 20 ± 5 fs and < 10 fs for the peaked and uniform components respectively (blue and green lines in panel **c)**). Summing up, the experimental results and the analysis of the emission angles clearly indicate that two electronic states are at play in the Fano resonance at 17.33 eV of N_2. While this result is in agreement with the previous *ab initio* calculations as mentioned earlier in the thesis, discrepancies between calculated and experimental resonance profiles remained [13].
This experiment suggests that the resonance profile is a result of a superposition between two electronic states, the $3d\pi_g$ and $4's'\sigma_g$, interacting via a common continuum. In the theoretical calculations, the molecular axis was kept fixed and thus no rotationally-induced couplings were included; furthermore, the theoretically calculated line widths do not correspond to the observed lifetimes of the electronic states. In a later published paper [27], modulations of the absorption profiles of N_2 with rotational temperature was observed, even though the experiments were not performed in the same energy range of this particular Fano resonance. Still, rotationally-induced couplings could be at play here as the rotations of the molecule could allow for symmetry-breaking coupling between the two states and continua of different symmetry. Therefore, the mixing of two discrete states via a common continuum, a known effect in literature

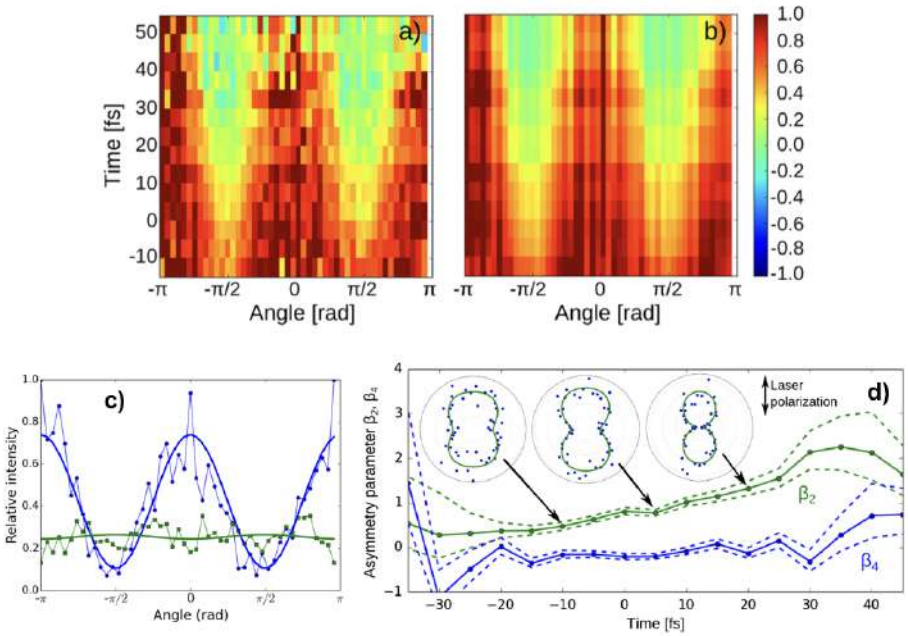

*Figure 2.5: Panel **a)** and **b)**: the angular distributions' integrated signal between 0.1 and 0.3 eV is shown as a function of time before (**a**) and after (**b**) SVD decomposition. Panel **c)**: the time-dependence of the asymmetry parameters $\beta_{2,4}$. Panel **d)**: the decay-associated signals to the angular distribution after SVD. All figures are taken from [5, 6].*

commonly called *interference stabilization* or *interference narrowing* [7, 10, 11, 37, 38], could explain the discrepancy between the widths and the decay times. When two closely lying resonances with overlapping width interact with a common continuum, provided that the coupling is sufficiently strong, they can be transformed into a system of two resonances located around the same energy, one of them being narrow (long lifetime) and the other one broad (short lifetime) [7]. Raoult's calculation indeed yield a separation between the $4s\sigma_g$ and $3d\pi_g$ resonances of just 40 meV, smaller than the 60 meV width of both [13]. Interference stabilization should then be at play and thus further investigation into the dynamics of the states from this point of view could resolve the discrepancies between theory and experiment while also providing a simple interpretation of the arising complex lineshape.

Chapter 3

Two-state interference stabilization

Introduction

In the previous two chapters, I have briefly overviewed the theory of autoionization in molecules and focused specifically on the Fano resonance of the "emission" series in the nitrogen molecule at 17.33 eV.
In this chapter, I will first introduce briefly the interference stabilization effect, focusing on the existing literature. I will then show how the effect, which was originally formulated for the case of two or more states coupled to one continuum, can be expanded to include additional continuum channels. Specifically, I will give analytical results for the case of two states coupled to an arbitrary number of continua and show what new effects and situations can be achieved. These results will be then applied in the final chapter, where I will show how the novel theory can be applied to the case of N_2. The results of this chapter and the next one were published in the Faraday Discussions [6].

3.1 Interference stabilization - a brief overview

The interference stabilization effect has been long known both experimentally and theoretically [7, 10, 11, 37, 38] and can be applied to different physical systems owing to its very general requirements. The most complete theoretical study of interference stabilization to date is the work done by Popov and Fedorov [7, 8, 10], where two or more discrete states are coupled to a common continuum.
Consider the system in figure 3.1. To explain this effect, we can focus just on the excited part of the system, i.e. we forget about the ground state for now. The two discrete states are separated in energy by $\Delta_E = |E_2 - E_1|$ and can both decay toward the continuum: the discrete-continuum coupling can be provided by the configuration interaction, like in autoionization, or also by external fields as in the case of laser induced continuum structure (LICS) [39]. Note that in the latter case the two states do not need to have an autoionizing character as the continuum can be reached by the one-photon laser-assisted transition. Nonetheless, regardless of the type of interaction

for the effect to occur we only need an available discrete-continuum transition for two or more states toward a common decay channel.
In an energy-domain picture, the two states have corresponding line profiles of the two resonances with a width given by the Fermi Golden Rule (FGR) [40, 41], i.e. $\Gamma_{nE} = 2\pi|V_{nE}|^2$, where I use atomic units and V_{nE} is the matrix element corresponding to the transition between the state $|n\rangle$ and the continuum $|E\rangle$. Provided that the states lie close in energy, the two profiles can overlap. Now, if the width of the resonances is bigger than their energy separation, i.e. when

$$\Gamma_{nE} > \Delta_E \tag{3.1}$$

a coherent repopulation of the bound states after ionization, owing to the transition $E_n \rightarrow E \rightarrow E_m$ (where E denotes the continuum) can occur. As a counter-intuitive result of the effect, the lifetime of one of the new eigenstates of the Hamiltonian, superposition of the field-free ones, increases for increasing value of Γ_{nE}. This fact can be easily seen from the perspective of the quasi-energies of the dressed systes: while the real part of the quasi-energies corresponds to the energy around which the resonances are centred, their imaginary part corresponds to their decay (figure 3.2). When the coupling strength is increased, after the branching point $\Gamma = \Delta_E$ the width of one of the eigenstates becomes increasingly smaller while the other one enlarges. Since the width of the line profiles is connected to their lifetime through $\tau = 1/\Gamma$, one of the superposition states becomes stabilized at the expense of the other.
The pioneering work by Fedorov, Popov and others, although already rich in interesting effects and conclusions, does not consider the more realistic case where the states are coupled to more than one continuum with different strenghts.
In the next section I thus include in the framework of the existing theory the case where a number N of continua are coupled to two discrete states and analyze the novel effects this generalization leads to.

3.2 Theory of interference stabilization

The following derivation follows the time-dependent approach I opted for in describing the interference stabilization effect in our recently published paper [6]. In this thesis work, I give a more comprehensive description and derivation of the effect, together with previously unpublished results.
The system I am considering is schematically depicted in figure 3.1. It consists of a ground state and two closely lying autoionizing states above the ionization potential. The AIS are supposed to be coupled to an arbitrary number of continua N. The system is initially in the ground state $|\phi_g\rangle$ and is excited by a ultrashort pulse at time $t_0 = 0$. The absorption of a photon leads to either direct ionization to any of the continuum channels E_j or excitation of the two AIS. The latter once populated can then decay to the continua with a rate $\Gamma = 2\pi|V_{nE}|^2$.
I will use the atomic units if not otherwise specified. The wavefunction of the system

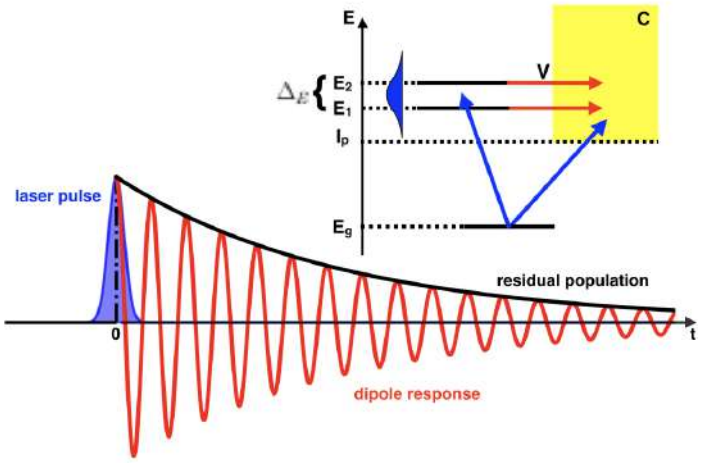

Figure 3.1: The dynamics of the system under study. An initial short and sufficiently broad laser pulse interacts with the ground state at time $t = 0$, populating the auto-ionizing states and inducing a time-dependent dipole response in the system, while directly transferring part of the population in the ionization continuum. The autoionizing (or dissipative) nature of the populated states results in a damped oscillatory response to the external field, which decays with a certain lifetime τ together with the remaining population in the bound-states. The reader must not be tricked into thinking that this picture represents the effect of interference stabilization, since the effect consists in an enlargement or shrinking of the lifetime of the states and induces substantial changes compared to the standard dynamics of a Fano resonance.

in the eigenstates of the field-free Hamiltonian is

$$|\Psi(t)\rangle = c_g(t)e^{-iE_g t}\,|\phi_g\rangle + e^{-i(E_g+\omega_{XUV})t}\left[\sum_{i=1,2} c_i(t)\,|\phi_i\rangle + \sum_{j=1}^{N}\int dE_j c_{E_j}(t)\,|\phi_{E_j}\rangle\right] \quad (3.2)$$

where I denote the continuum by E_j. E_g and ω_{XUV} are respectively the ground state energy and the frequency of the XUV pulse. In this thesis work, I will try to model only the static absorption of a photon: the Hamiltonian of the system is thus

$$H(t) = \hat{H}_0 + \hat{V} - \hat{d}\cdot\mathcal{E}_{XUV}(t) \quad (3.3)$$

where $\hat{H}_0$ is the 'free' Hamiltonian, $\hat{V}$ the configuration interaction coupling the discrete states $|i\rangle$ to the continua and $\hat{d}$ and $\mathcal{E}_{XUV}(t)$ are the dipole operator and the XUV field. The latter is taken to be

$$\mathcal{E}_{XUV}(t) = F_{XUV}f(t)e^{i\omega_{XUV}t} + c.c. = A_{XUV}(t)e^{i\omega_{XUV}t} + c.c. \quad (3.4)$$

where $|F_{XUV}|^2$ is the peak intensity of the field and $f(t)$ is the time-dependent pulse envelope. In order to reconstruct the dynamics, one has to solve the time-dependent

Schrödinger equation

$$\mathrm{i}\partial_t \left|\Psi(t)\right\rangle = \hat{H}(t) \left|\Psi(t)\right\rangle \tag{3.5}$$

Inserting the wavefunction (3.2) in the TDSE and using the Rotating Wave Approximation (RWA), we can ignore the fast oscillation of the counter-rotating terms of the XUV field and obtain the following system of coupled differential equations for the probability amplitudes:

$$\mathrm{i}\dot{c}_g(t) = -\sum_i c_i(t)\frac{d_{gi}}{2}A_{XUV}(t) - \sum_j \int dE_j c_{E_j}(t)\frac{d_{gE_j}}{2}A_{XUV}(t) \tag{3.6}$$

$$\mathrm{i}\dot{c}_i(t) = \Delta_i c_i(t) - c_g(t)\frac{d_{ig}}{2}A^*_{XUV}(t) + \sum_j \int dE_j c_{E_j}(t)V_{iE_j} \tag{3.7}$$

$$\mathrm{i}\dot{c}_{E_j}(t) = \Delta_{E_j} c_{E_j}(t) - c_g(t)\frac{d_{E_j g}}{2}A^*_{XUV}(t) + \sum_i c_i(t)V_{E_j i} \tag{3.8}$$

where I have set $E_g = 0$ and $d_{ig} = \langle i|\,\hat{d}\,|g\rangle$, $V_{iE_j} = \langle i|\,\hat{V}\,|E_j\rangle$ are the dipole and configuration interaction matrix elements and $\Delta_i = E_i - \omega_{XUV}$, $\Delta_{E_j} = E_j - \omega_{XUV}$ are the detunings. The latter are then included in the transformation $a_i(t) = c_i(t)e^{i\Delta_i t}$. The resulting system of integro-differential equations does not have a straightforward analytical solution. I will thus proceed by *adiabatically eliminating the continuum*, a common approximation in literature when dealing with such systems [6, 7, 10]. This is done by first formally integrating the continuum amplitudes as follows

$$a_{E_j}(t) - a_{E_j}(t_0) = \mathrm{i}\int_{t_0}^{t} dt' c_g(t')\frac{d_{E_j g}}{2}A^*_{XUV}(t')e^{i\Delta_{E_j}t'} - \mathrm{i}\int_{t_0}^{t} dt' \sum_i a_i(t')V_{E_j i}e^{i(\Delta_{E_j}-\Delta_i)t'} \tag{3.9}$$

where, if the system was initially in the ground state, $a_{E_j}(t_0) = 0$. The latter expression is then substituted into the equations for the ground and discrete states. The adiabatic approximation consists in assuming that the continuum is *flat*, i.e. the dipole matrix element coupling the states to the continua do not depend on the energy E_j. This allows one to change the order of integration once the matrix elements are taken out of the integration over the continuum energies. The resulting integral over the energies is

$$\int_{I_{p_j}}^{\infty} dE_j e^{\mathrm{i}\Delta_{E_j}(t'-t)} \tag{3.10}$$

where I_{p_j} is the ionization threshold. By changing the variable from the continuum energy to the detuning Δ_{E_j}, we would have an integral over the range $[I_{p_j} - \omega_{XUV}, \infty]$. Taking in account that I want to model the photoelectron experiment N_2 experiment, where the XUV photon energy was 17.5 eV, we are therefore roughly 2.2 eV above the ionization threshold of N_2. The integrand thus oscillates with a period of around 1.9 fs. Since we are not interested in such fast dynamics, we can safely let the lower

integration limit go to $-\infty$. This results in terms proportional to $2\pi\delta(t'-t)$, which then give the following equations for the amplitudes of the discrete states:

$$\mathrm{i}\dot{c}_g(t) = -\sum_i a_i(t)e^{-i\Delta_i t}A_{XUV}(t)\frac{d_{gi}}{2}\left(1-\frac{\mathrm{i}}{q_i}\right) - \mathrm{i}c_g(t)\sum_j \pi|d_{E_j g}\cdot A_{XUV}(t)|^2 \quad (3.11)$$

$$\mathrm{i}\dot{a}_i(t) = -c_g(t)e^{i\Delta_i t}A^*_{XUV}(t)\frac{d_{ig}}{2}\left(1-\frac{\mathrm{i}}{q_i}\right) - \mathrm{i}a_i(t)\sum_j \Gamma_{ij} - \mathrm{i}a_l(t)e^{-i(\Delta_l-\Delta_i)t}\sum_j \Gamma_{ijl} \quad (3.12)$$

where $l \neq i$ refer to the discrete states and I have introduced the rates associated with the different transitions:

$$\Gamma_{ij} = 2\pi|V_{iEj}|^2 \qquad |i\rangle \to |E_j\rangle \quad (3.13)$$

$$\Gamma_{ijl} = 2\pi V_{iE_j}V_{E_j l} \qquad |i\rangle \to |E_j\rangle \to |l\rangle \quad (3.14)$$

It is clear that while the bound state $|\phi_i\rangle$ decays in time at a total rate $\Gamma_i = \sum_j \Gamma_{ij}$, it also interacts with the other resonance via $\Gamma_{il} = \sum_j \Gamma_{ijl}$. Furthermore, I have also introduced the Fano asymmetry parameters [2]:

$$q_i = \frac{d_{gi}}{2\pi\sum_j d_{gE_j}V_{iE_j}} \quad (3.15)$$

which give an estimate of the relative strength between the direct and indirect transitions. Notice that the total Fano parameter q_i can be expressed as a sum of the parameters for each continuum channel q_{ij} as

$$q_i = \left(\sum_j \frac{1}{q_{ij}}\right)^{-1} \quad (3.16)$$

$$q_{ij} = \frac{d_{gi}}{2\pi d_{gE_j}V_{iE_j}} \quad (3.17)$$

Up to now I did not specify the temporal shape of the field $f(t)$. If the pulse is assumed to be very short in time compared to the relevant timescales of the system, it looks reasonable to model it as a δ-like pulse, that is $\mathcal{E}_{XUV}(t) = F_{XUV}\delta(t)e^{i\omega_{XUV}t} + c.c.$ Assuming that the ground state is left mostly unperturbed by the XUV pulse, we can set $c_g(t) \simeq c_g(t_0 \to -\infty) = 1$. The evolution of the bound state amplitudes may then be expressed as

$$a_i(t) = \begin{cases} 0 & \text{for } t \leq 0 \\ a_i(t) & \text{for } t > 0 \end{cases} \quad (3.18)$$

where the initial conditions set by the field are

$$a_i(t \to 0) = \mathrm{i}F_{XUV}\frac{d_{ig}}{2}\left(1-\frac{\mathrm{i}}{q_i}\right) \quad (3.19)$$

For later times $t > 0$, the evolution is governed by the decay toward the continuum:

$$\mathrm{i}\dot{a}_i(t) = -\mathrm{i}a_i(t)\sum_j \Gamma_{ij} - \mathrm{i}a_l(t)e^{-i(\Delta_l-\Delta_i)t}\sum_j \Gamma_{ijl} \tag{3.20}$$

where $l \neq i$ and $i = 1, 2$. The system can now be solved by looking for a non-trivial solution of the form $a_i(t) = f_i e^{i(\Delta_i-\gamma)t}$, which leads to a quadratic equation for the quasi-energies γ having solutions

$$\gamma_\pm = \frac{1}{2}\left[(E_1 + E_2) - \mathrm{i}(\Gamma_1 + \Gamma_2) \pm \sqrt{\Delta}\right] \tag{3.21}$$

$$\Delta = \left[\Delta_E + \mathrm{i}(\Gamma_2 - \Gamma_1)\right]^2 - 4\left(\sum_j \sqrt{\Gamma_{1j}\Gamma_{2j}}\right)^2 \tag{3.22}$$

where Δ_E is the energy separation of the quasi-bound states. Due to the presence of dissipative terms $\mathrm{i}\Gamma$, the population of the bound-part of our system is in general not preserved and the quasi-energies of the non-Hermitian Hamiltonian $\gamma_\pm$ are complex quantities. Their interpretation can be easily understood given that their real part represents the energy around which the associated resonances are centered while the imaginary part is related to the width of such resonances (or from a time-domain perspective, to the inverse of their lifetime). Therefore, the smaller the imaginary part, the sharper the resonance and the longer the associated decay time.
To understand the effect of interference stabilization, it is important to notice that when the total rate exceeds the energy gap, i.e. when $\Gamma > \Delta_E$, the square root term becomes purely imaginary and will therefore contribute only to the decaying part of the amplitudes, effectively shrinking the width of one of the resonances while making larger the other one. For increasing coupling strength, this results in the stabilization against ionization of one of the resonances. This effect is precisely the so-called *interference stabilization* phenomenon.

3.2.1 Balanced and unbalanced cases of interference stabilization

Now that the expressions for the quasi-energies of the system are known (equation 3.21), we have the tools to analyze their dependence on the rates Γ_{ij}, that is the configuration interaction that leads to the decay of the AIS. It is interesting therefore, following Fedorov and Popov treatment [7, 10], to plot the quasi-energies as a function of the total rate $\Gamma = \sum \Gamma_{ij}$ and analyze the different possible effects that arise in such a system.
In the simplest case, the coupling strengths of the two states are the same to all continua, i.e. $\Gamma_{ij} = C$ (where C is a constant) and $\Gamma_1 = \Gamma_2$. In this case, there is nothing differentiating one continuum channel from the other and the system behaves as if there was just one continuum. In panel **a)** of figure 3.2, the system behaves

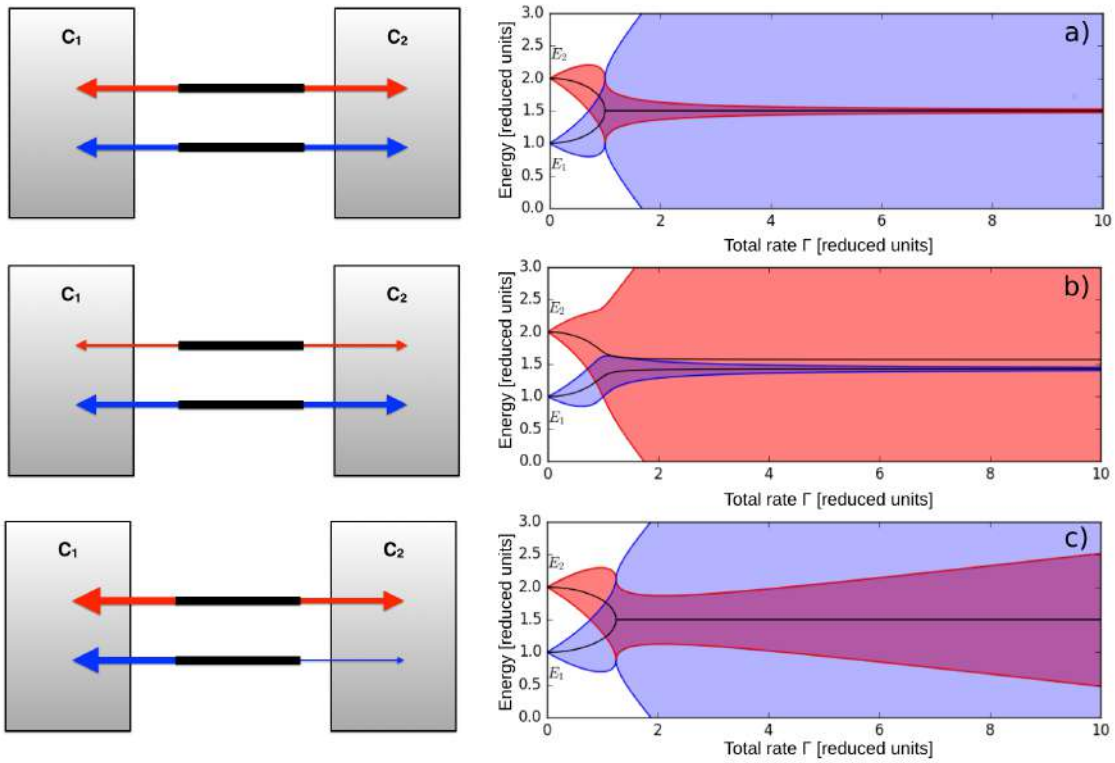

*Figure 3.2: Left: schematic diagrams depicting the three cases of interference stabilization. The size of the arrows is meant to represent the strength of the interaction. Right: resonance positions $Re(\gamma_\pm)$ (black dotted line) and effective resonance boundaries $Re(\gamma_\pm) \pm Im(\gamma_\pm)$ (red and blue shaded regions) for three sets of parameters describing two discrete states coupled to two continua, plotted against the total rate Γ. a) **Balanced case**: the two discrete states have identical coupling strengths to the two continua, i.e. $\Gamma_{1E_1} = \Gamma_{2E_1}$ and $\Gamma_{1E_2} = \Gamma_{2E_2}$. b) **Partially balanced case**: the coupling strengths of both discrete states to the two continua are balanced ($\Gamma_{1E_1} = \Gamma_{1E_2}$ and $\Gamma_{2E_1} = \Gamma_{2E_2}$), but the one resonance is coupled to the continua weaker than the other one ($\Gamma_1 < \Gamma_2$). c) **Unbalanced case**: the coupling constants of two discrete states are different for each continuum.*

exactly as reported already in literature [7], confirming the correctness of our results. I denote this case as ***balanced case***. In a more realistic case though, the coupling strength between the AIS and the continua are not the same. This leads us to two possible configurations: the ***partially balanced*** and ***unbalanced*** cases of interference stabilization.

In the first one, the coupling strength of each AIS is the same for all continua, but their total rates differ. That is, $\Gamma_1 \neq \Gamma_2$ but $\Gamma_{ij} = \Gamma_{iC}\ \forall j$. In the latter case instead, the coupling strength of the AIS are different for each continuum. The corresponding diagrams and quasi-energies plots, showing the width and the resonance positions of the states as a function of the total rate Γ, for all three possible configurations of two AIS coupled to two continua are shown in figure 3.2.

While in the balanced case the resonance positions merge when the branching point $\Gamma = \Delta_E$ is reached, in the partially balanced case the stabilization still takes place but the two resonances are separated by $|2\mathrm{i}\Delta_E(\Gamma_1 - \Gamma_2)|$. Finally, in the unbalanced case after an initial shrinking the width of the quasi-energy zone reaches a minimum and then becomes larger again.
It is also possible to derive an expression for the minimum of the resonances' width for the unbalanced configuration when $\Gamma_1 = \Gamma_2$:

$$\Gamma_{\min} = \left(\frac{\Delta_E^2}{4(\sum_j \sqrt{R_{1j}R_{2j}})^2 - 16(\sum_j \sqrt{R_{1j}R_{2j}})^4} \right)^{1/2} \tag{3.23}$$

where $\Gamma_{ij} = R_{ij}\Gamma$, R_{ij} being a branching ratio. This result can be useful as one could think of tuning the interaction between discrete and continuum states by means of a laser field and optimally controlling the lifetime of the resonances under study. It is also easy to check that for the case where $\Gamma_{1j} = \Gamma_{2j}$ ($R_{1j} = R_{2j}$), the minimum position is $\Gamma_{\min} \to \infty$ as one would expect.

3.2.2 Time-evolution of the bound states' populations

To give a complete picture of the three cases of interference stabilization, we have to look at the probability amplitudes of the discrete states. Expressing the initial field-free states in the basis of the eigenstates of the Hamiltonian, we find that

$$c_i(t) = \sum_{\alpha=\pm} C_\alpha A_i^\alpha e^{-\mathrm{i}\gamma_\alpha t} \tag{3.24}$$

where the amplitudes A_i^α and the constants C_α are given by

$$A_1^\pm = -\mathrm{i} \tag{3.25}$$

$$A_2^\pm = \frac{1}{2}\frac{\Delta_E - i(\Gamma_1 - \Gamma_2) \pm \sqrt{\Delta}}{\sum_j \sqrt{\Gamma_{1j}\Gamma_{2j}}} \tag{3.26}$$

$$C_+ = \frac{c_1(0)A_2^- - c_2(0)A_1^-}{A_2^-A_1^+ - A_2^+A_1^-} \tag{3.27}$$

$$C_- = \frac{c_2(0)A_1^+ - c_1(0)A_2^+}{A_2^-A_1^+ - A_2^+A_1^-} \tag{3.28}$$

The time evolution of the amplitudes can be written in term of an evolution operator as follows:

$$\begin{pmatrix} c_1(t) \\ c_2(t) \end{pmatrix} = e^{\frac{i}{2}(\Delta_1+\Delta_2)t} e^{-\frac{\Gamma}{2}t} U(t) \begin{pmatrix} c_1(0) \\ c_2(0) \end{pmatrix} \tag{3.29}$$

where the matrix elements of $U(t)$ are

$$U_{11} = \cos(\Omega t) + \frac{\mathrm{i}\alpha}{\Omega}\sin(\Omega t) \tag{3.30}$$

$$U_{12} = \Gamma_{12}\frac{\sin(\Omega t)}{\Omega} \tag{3.31}$$

$$U_{21} = -\Gamma_{12}\frac{\sin(\Omega t)}{\Omega} \tag{3.32}$$

$$U_{22} = \cos(\Omega t) - \frac{\mathrm{i}\alpha}{\Omega}\sin(\Omega t) \tag{3.33}$$

and $\Omega = \sqrt{\Delta}/2 = \sqrt{\alpha^2 - 4\Gamma_{12}^2}/2$, $\alpha = \Delta_E + \mathrm{i}(\Gamma_2 - \Gamma_1)$. Taking the limit of small coupling, i.e. $\Gamma_{12} \ll \Delta_E$, it is possible to verify that the above equations reduce to the case of two single autoionizing resonances decaying at corresponding rates Γ_i when the interference stabilization effect vanishes.
The frequency Ω clearly affects the evolution of the amplitudes: before the branching point, in the simplest case of $\Gamma_1 = \Gamma_2$, Ω is a real quantity and therefore affects only the position of the resonances, resulting in a phase factor that has no effect on the populations. For $\Gamma \geq \Delta_E$, Ω becomes an imaginary quantity and effectively affects the decay rate Γ. Larger values of $|\Omega|$ in this case lead to a slower decay; in the limit of big Ω, one can verify that half of the population is lost toward the continuum while the other half remains trapped between the two resonances.
In figure 3.3, I report the time-evolution of the populations in the auto-ionizing states corresponding to the three cases of interference stabilization for increasing total rate Γ. The stabilization effect can be directly seen by looking at the decay times of the dressed states, i.e. $\tau^{\pm} = 1/\Gamma^{\pm}$: in the balanced and partially balanced cases, the decay τ^{+} becomes an increasing function of the total rate Γ once the branching point is passed; notice that in the first case the width of the resonances coincide until $\Gamma = \Delta_E$. In the unbalanced case however the rate τ_{+} is an increasing function of Γ only for a small interval after the branching point.
The resulting initial populations reflect these qualitative observations in the plots on the left side. In the balanced case, we are quickly brought to an equal distribution of the population in the two states which decay together at the same rate. In the limit of very large Γ, half of the population is lost and half is trapped between ϕ_1 and ϕ_2. In the partially balanced case, due to the difference between the total couplings Γ_i, the widths of the resonances are not equal at the branching point. In fact, the lifetime of the stabilized dressed state increases faster than in the balanced case.

3.2.3 Photoelectron spectrum

Using the AIS amplitudes expressed in the dressed states basis (equation 3.24), we can now find the explicit time-dependence of the continuum amplitudes using equation 3.9.

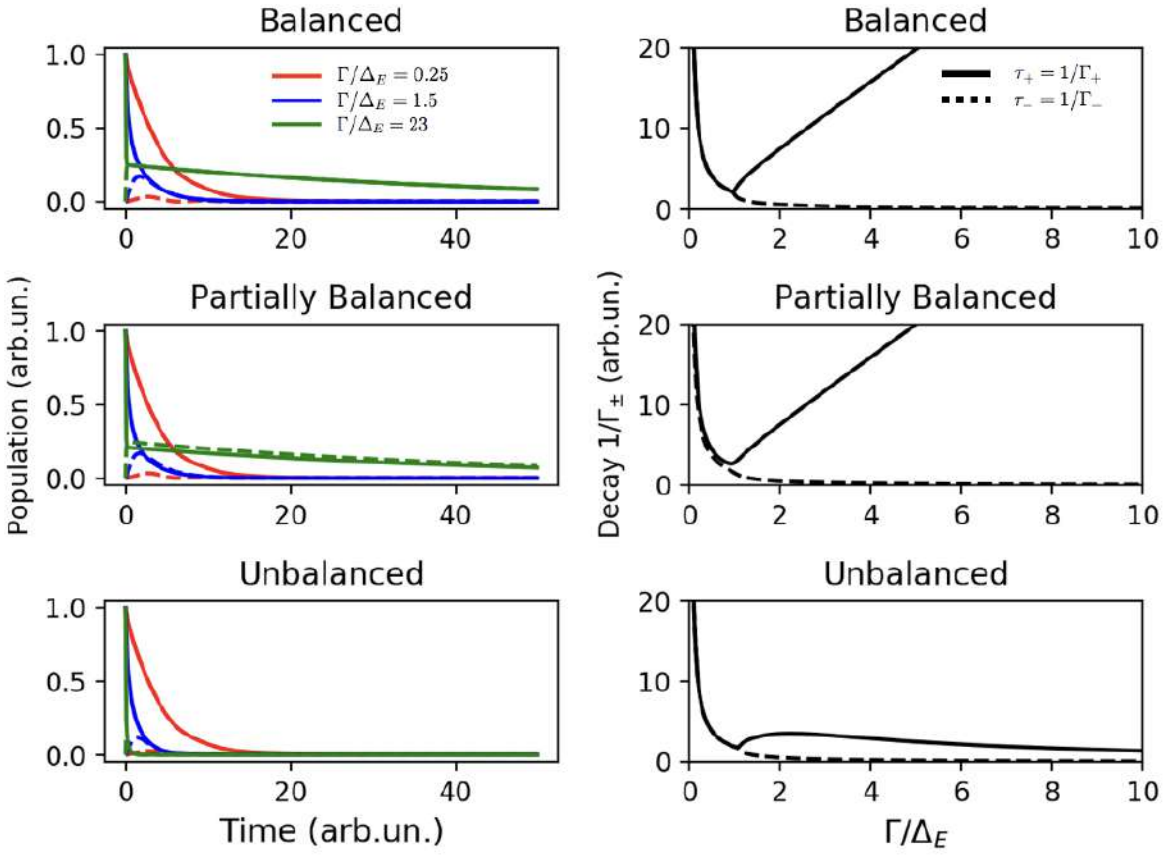

Figure 3.3: Time-dependent populations and decays of the initial field-free and dressed states respectively for the three different configurations of interference stabilization and initial conditions $c_2(0) = 1$, $c_1(0) = 0$. The solid (dashed) lines on the left correspond to $c_1(t)$ ($c_2(t)$). On the right, the dressed-state associated decays $\tau^{\pm} = 1/\Gamma^{\pm}$ are plotted in function of Γ/Δ_E.

This yields

$$c_{E_j}(t) = \mathrm{i}e^{-i\Delta_{E_j}t}\left[\frac{d_{E_j g}}{2} + \sum_i V_{E_j i}\sum_\alpha \frac{C_\alpha A_i^\alpha}{\mathrm{i}(\Delta_{E_j} - \gamma_\alpha)}\left(1 - e^{-i(\gamma_\alpha - \Delta_{E_j})t}\right)\right] \tag{3.34}$$

The photoelectron spectrum is in turn given in the detection limit $t \to \infty$ by

$$P_E = \lim_{t\to\infty}\sum_j |c_{E_j}(t)|^2 \tag{3.35}$$

To analyze the effect of interference stabilization on the photoelectron spectrum, we forget about the Fano picture by neglecting the interference effect between the direct and indirect ionization. Accordingly, I assume that the continuum is empty at initial times and neglect the first term on the RHS of equation 3.34, setting to fixed values the initial conditions for the discrete states $c_i(0)$. The resonance profiles are thus

Lorentzians.
In figure 3.4, I set $c_1(0) = c_2(0)$ and report the photoelectron spectrum for the three cases of interference stabilization for two states coupled to two continua. In all three cases a sharp drop in probability is observed after $\Gamma = \Delta_E$ around the resonance energy corresponding to the stabilized state. As expected, the width of the dip evolves according to the quasi-energy plots, shrinking in the balanced and partially balanced case for increasing couplings and getting larger after the point of minimum width in the unbalanced one. In the partially balanced case, where the total coupling strengths Γ_i differ from one another, the shift from the middle point is also observed as predicted. Although stabilization is clearly occurring in all three cases, the population in the continuum is distributed over the unstable state - the broader resonance on top of which the dip sits. Therefore, only the fast-decaying superposition of field-free states is populated. To take advantage of the stabilization against ionization, we therefore

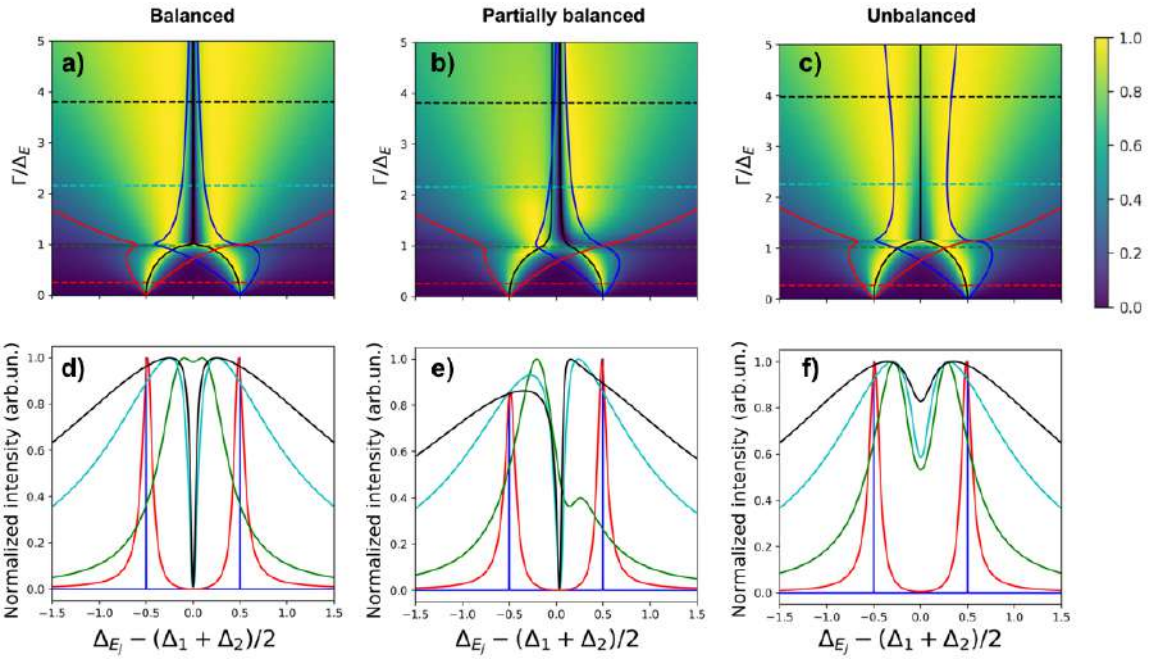

*Figure 3.4: Photoelectron spectrum for the balanced (**a**), partially balanced (**b**) and unbalanced (**c**) cases. In all plots the zero of the x-axis corresponds to the mean energy between the two resonances. In the plots on the top, the normalized spectrum as a function of the reduced total rate Γ/Δ_E is plotted as a false color map. The quasi-energy zones are plotted on top of the spectrum as solid blue and red lines. The dotted lines which correspond to cuts through the spectrum at a fixed total rate, correspond in color to the lineshapes in **d**, **e** and **f**.*

need to populate the slowly decaying superposition. This can be done by inducing a phase shift between the initial amplitudes of the field-free states, which changes the projection of the states on the dressed basis.
In figure 3.5 I report for the balanced case the residual population $w_{res}(t) = \sum_i |c_i(t)|^2$ for a fixed total rate $\Gamma/\Delta_E = 4$ and varying phase difference $\Delta\phi$ between the two

discrete states at initial times. The plot clearly shows that by changing the phase difference from 0 to π the residual population decays at a slower pace. For comparison, the inset shows the dressed states decay $e^{-\Gamma_{\pm}t}$. In figure 3.6, the real and imaginary part of the terms $C_\alpha A_i^\alpha = B_i^\alpha$, i.e. the components of the discrete states amplitudes on the dressed basis, are shown as a function of the total rate Γ/Δ_E for the limiting cases $\Delta\phi = 0, \pi$. Blue and red markers correspond respectively to the discrete states $|1\rangle$ and $|2\rangle$ while crosses and squares correspond to the dressed states $|+\rangle$ and $|-\rangle$. When $\Delta\phi = 0$, for large values of Γ/Δ_E the only non-zero projections are B_i^-, i.e. only the fast-decaying dressed state $|-\rangle$ is populated. This would correspond to the balanced case of the photoelectron spectrum of figure 3.4. When $\Delta\phi = \pi$ instead, the projections B_i^- approach zero for large Γ/Δ_E while the projections B_i^+ approach an asymptotic non-zero value. This shows that only the slow decaying state is populated when a π shift between the initial amplitudes is present.
This is an interesting result as I clearly show that by changing the relative phases between the initial discrete states one can selectively populate the long or short lived state. One could for example think of coupling off-resonantly the two states to a third one via an additional field and achieve in this way control of the relative phases and thus the profile of the photoelectron spectrum. Although I show here only the case of two Lorentzian profiles, the effect should occur for a Fano system as well. In the next section, I will show indeed that opposite or equal Fano prameters result in different absorption profiles.

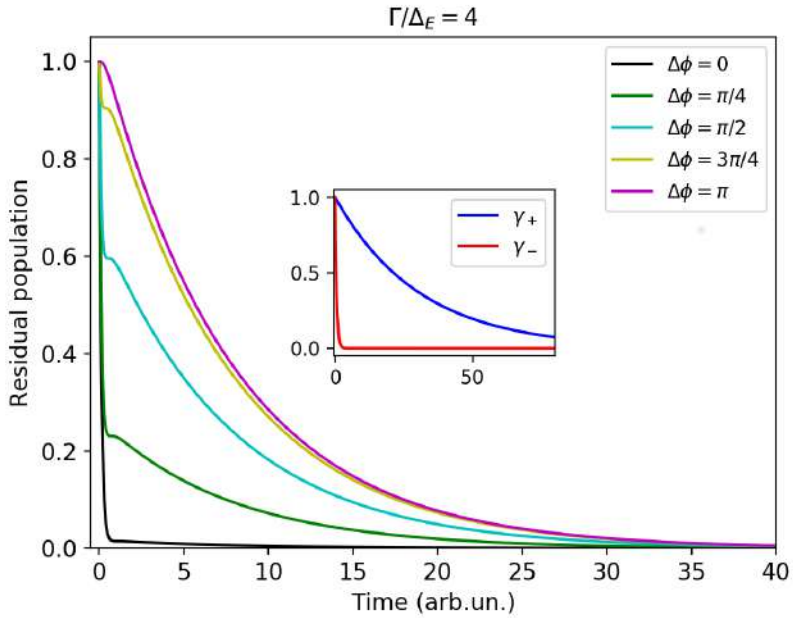

Figure 3.5: The residual population in the bound states $w_{res}(t) = \sum |c_i(t)|^2$ for the rate $\Gamma/\Delta_E = 4$ and different phase differences $\Delta\phi$ between the discrete states. The inset shows the decay of the fast and slow decaying dressed states.

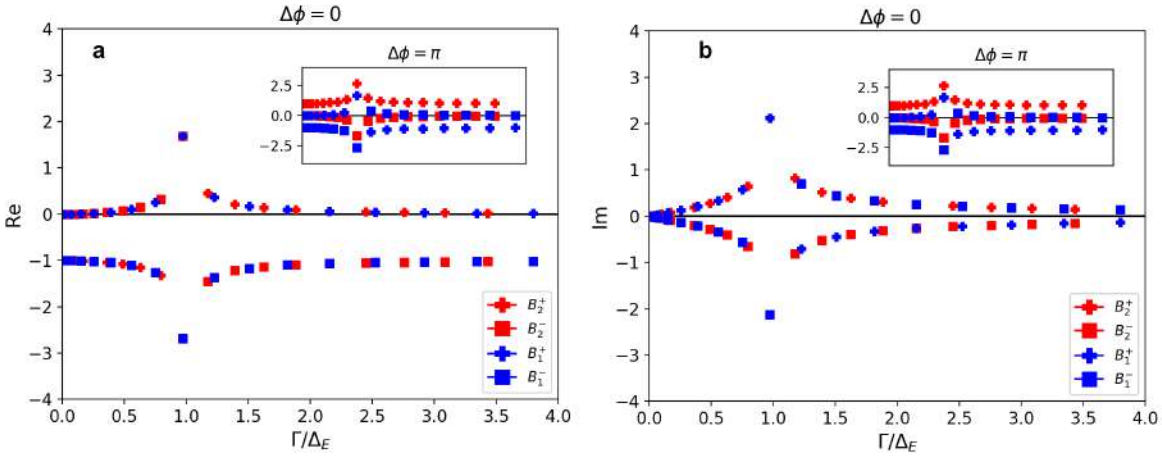

*Figure 3.6: The real (**a**) and imaginary (**b**) part of the amplitudes $C_\alpha A_i^\alpha = B_i^\alpha$ as a function of the total reduced rate Γ/Δ_E for $\Delta\phi = 0, \pi$.*

3.2.4 Absorption spectrum

In order to find the absorption spectrum, one can use the optical theorem which relates the absorption cross section to the imaginary part of the dipole spectrum in the frequency domain:

$$\sigma_{abs}(\omega) \propto \mathrm{Im}\left[\tilde{d}(\omega)\right] \tag{3.36}$$

We thus proceed to find the dipole response in the time-domain, defined as $d(t) = \langle\Psi(t)|\,\hat{H}\,|\Psi(t)\rangle$. Separating our wavefunction as $\Psi = \Psi_g + \Psi_{ex}$, where Ψ_{ex} accounts for the discrete and continuum states, we find for the dipole moment $\langle\Psi_g|\,\hat{H}\,|\Psi_{ex}\rangle$

$$d(t) = \left[\mathrm{i}\frac{\Gamma_{gC}}{2}\delta(t) + \sum_{i,\alpha} C_\alpha A_i^\alpha e^{-i\gamma_\alpha t}\frac{d_{gi}}{2}\left(1 - \mathrm{i}/q_i\right)\right]\Theta(t) \tag{3.37}$$

We then take the Fourier transform of this expression and find the absorption spectrum of our system. We report the absorption spectrum for the balanced case of interference stabilization in figure 3.7. In the panels **a)** and **c)** of the plot, the two resonances have equal Fano parameters $q_1 = q_2$ while in panels **b)** and **d)** the parameters are opposite $q_1 = -q_2$. The resulting resonance profile in the regime of stabilization clearly changes depending on the q parameters, which determine the initial conditions for the amplitudes as expressed in equation 3.19. Therefore changing the sign of the Fano parameter corresponds to changing the phase of the amplitude by a factor of π as in the previous chapter. When the Fano parameters are the same, the profile has two points of destructive interference around an asymmetric central peak whose width shrinks as Γ is increased. This double-zero profile is in accordance with the existing literature [42]. In the case of opposite q parameters instead, the resulting central peak is symmetric due to the two tails of the initial Fano profiles.

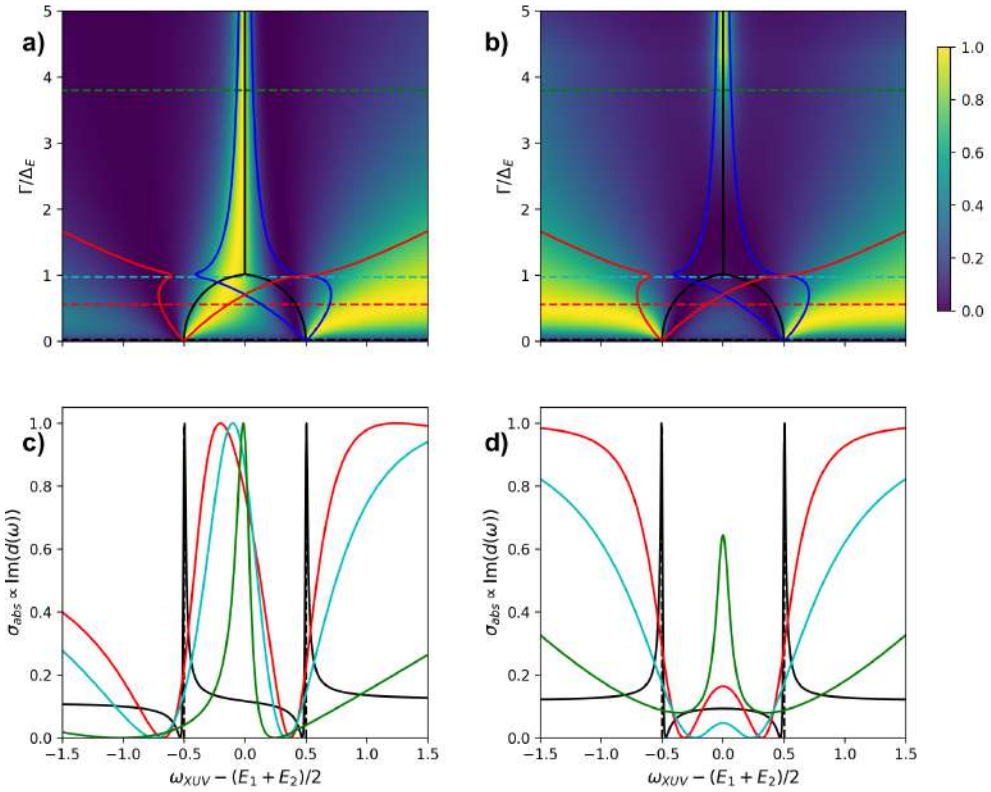

*Figure 3.7: Absorption spectrum for the case of two Fano profiles with equal (**a** and **c**) and opposite (**b** and **d**) signs of the Fano parameters. The figures **a** and **b** are false color plots of the profiles as a function of the total rate Γ/Δ_E, while the plots **c** and **d** are cuts through the maps corresponding to the dashed lines in **a** and **b**.*

In conclusion, in this chapter I showed how the interference stabilization theory can be extendend to include the case of an arbitrary number of continua coupled to two discrete states. Novel theoretical results include the partially balanced and unbalanced case of interference stabilization; furthermore, I showed how the stabilization effect maps onto the time-dependent populations and absorption and photoelectron spectrum of the system. Moreover, by changing the relative phase between the discrete amplitudes, one can selectively excite the slow or fast-decaying dressed state and take full advantage of the interference stabilization effect. To clearly point out the interference stabilization effect, I decided to provide qualitative plots.
In the next chapter, I will show how the interference stabilization effect in autoionization can be applied to the Fano resonance of N_2 at 17.33 eV which can be modeled as two states coupled to four continua.

Chapter 4

Interference stabilization in N_2

In the previous chapter I have introduced the effect of interference stabilization in the case of two discrete states coupled to a number of continua. Compared to the existing literature, the inclusion of additional continua adds complexity to the system. I have then shown how the quasi-energy zones of the dressed system maps onto the population of the bound states and the photoelectron and absorption spectrum. The latter are two quantities which can be compared to the experiment, providing a benchmark for the theoretical predictions. In this section, I will show how the theory of interference stabilization was applied in one recent publication to the Fano resonance of N_2 at 17.33 eV [6].

4.1 Theoretical model

As previously mentioned, theoretical predictions and experimental results point at the presence of two overlapping resonances contributing to the resonance at 17.33 eV in N_2, the $3d\pi_g$ and the $4's'\sigma_g$ members of the Rydberg series converging to the $(B^2\Sigma_u^+)$ threshold [5,13,27]. The *ab initio* paper from 1983 assigned the dominant contribution to the $3d\pi_g$ state, which is coupled to the $X^2\Sigma_g^+$ and $A^2\Pi_u$ continua of the ion N_2^+. Due to the space-fixed molecular frame in which the theoretical calculations were done, the symmetry of the electronic wavefunction associated with the excited Rydberg state is preserved in the autoionization process and thus the $3d\pi_g$ state is coupled to the $X\Pi$ and $A\Pi$ continua. Similarly, the $4's'\sigma_g$ state is coupled to the $X\Sigma$ and $A\Sigma$ continua. The coupling strength, the resonance energy and the Fano parameters for the partial cross sections extracted from the fitted theoretical curves in [13] are reported in the table 4.1. It is clear that while the theoretical results predict the resonances widths to be similar, this fact is contradicted by the experimental results which show two states having substantially different lifetimes as shown in the previous chapter [5]. Yet, in the experiment on gas-phase N_2 the molecular frame is not fixed. That is, the N_2 molecule can freely rotate leading to autoionizing transitions involving changes in the rotational states of the molecule. This conclusion is indeed supported by

another experimental paper from 1993, where the Hopfield series of N_2 was investigated at room temperature and in rotationally-cold jets [27]. In the article, Huber et al. point out that at high rotational temperatures the coupling of the angular momentum of the electron becomes weaker than the rotational coupling. As a result, the Rydberg states can not be described anymore by the angular momentum projection on the molecular axis Σ and acquire a mixed Σ/Π character, leading to their coupling to ionization continua of different symmetry. This series of observations is the starting point of our application of the theory of interference stabilization effect to the case of this autoioinizing resonance: we model the autoionizing process by considering two states ($3d\pi_g$ and $4's'\sigma_g$) coupled to four continua ($X\Pi$,$A\Pi$,$X\Sigma$,$A\Sigma$). While the couplings between states and continua of same symmetry are set to the values in table 4.1, the couplings between the ground state and the four continua can be extracted from the q-parameters. The only remaining free parameters are the ratio between the dipole matrix elements between ground state and discrete states d_{g1}/d_{g2} and the symmetry-breaking rotational couplings.

$3d\pi_g$	$X\Pi$	$A\Pi$
E_0[eV]	17.35	17.35
Γ[meV]	63	74
q	1.18	0.37
$4's'\sigma_g$	$X\Sigma$	$A\Sigma$
E_0[eV]	17.405	17.35
Γ[meV]	63	88
q	-1.08	4.87

Table 4.1: Theoretical parameters extracted from figure 5 of Ref. [13].

4.2 Theoretical results

From equation 3.36, we calculate the absorption spectrum and set the ratio d_{g1}/d_{g2} such that our curve matches Raoult's one when interference stabilization is not taken in account (figure 4.1). We then proceed to include the rotational couplings by setting them equal to each other and scaling them from 0 to 25 meV, for a maximum total rotational coupling Γ_{rot} of 100 meV. The quasi-energy plot of the two states is shown in figure 4.1. Note that even for small rotational couplings, the resonances position shift substantially and for a total rotational coupling of 25 meV their widths' ratio (corresponding to the inverse of their lifetimes) exceeds two. However, to match the experimental results by Morin et al. [14] and resolve the discrepancies between theory and experiment, it is sufficient to vary the rotational couplings between 0 and 1 meV (figure 4.1).

Our theoretical results suggest that the $4's'\sigma_g$ state is stabilized by the rotationally-induced couplings as, in a two-state picture, the weakly coupled state undergoes stabilization. This is confirmed by the experimental results discussed at the end of the previous chapter: there, the long-lived component had a large asymmetry parameter, corresponding to the emission of an electron from an s-type orbital in the one-photon ionization by the linearly polarized XUV. The fact that the $4's'\sigma_g$ state has smaller rotational couplings than the $3d\pi_g$ is indeed nothing strange: due to the spherical symmetry of a s-type orbital, rotations of the molecular axis should not lead to any

change of the distribution, rendering a effectively rotationally-decoupled state. On the other hand, the d-type orbital is symmetric with respect to the molecular axis and should therefore follow its rotations. This then induces stronger rotational couplings and hence leads to destabilization.
In conclusion, the inclusion of the interference stabilization effect can explain the existing discrepancies between theory and experiment in the autoionization of the Fano resonance at 17.33 eV in N_2. Although the symmetry-breaking rotational couplings are two orders of magnitude smaller than the symmetry-allowed ones, substantial differences in the resonance absorption profile are observed nonetheless.

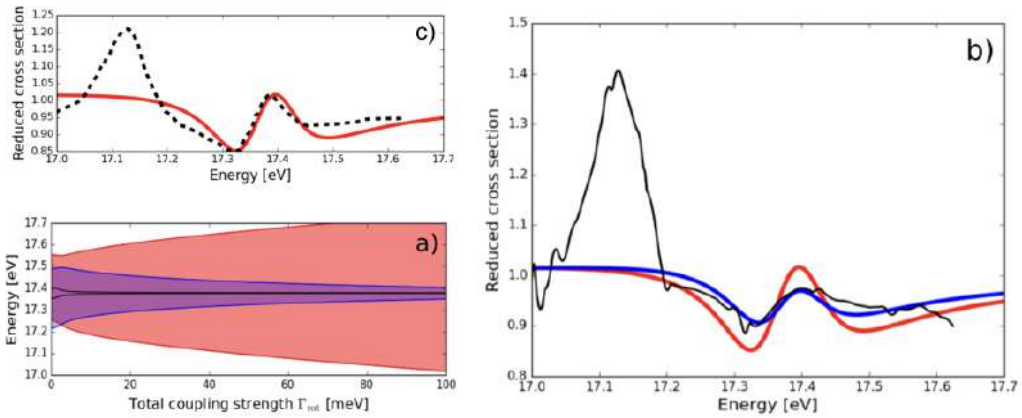

Figure 4.1: Panel ***a)****: quasi-energy zones plot for the* $3d\pi_g$ *(red shade) and* $4's'\sigma_g$ *(blue shade) states in function of the total rotational coupling* Γ_{rot}*, where the black lines represent the resonance positions. The resonance have a non-vanishing width when* $\Gamma_{rot} = 0$ *due to the symmetry-allowed couplings. Panel* ***b)****: the experimental XUV absorption curve from Morin et al. [14] (solid black line) and the calculated profile from this thesis work with and without interference stabilization (blue and red solid lines respectively). Panel* ***c)****: the calculated XUV absorption profile taken from [13] (dotted black line) and from this thesis work (solid red line) when no interference stabilization is included. The absorption resonance is not included in our treatment and can be neglected due to the large energy separation from the resonance at 17.33 eV. All images are adapted from [6].*

Chapter 5

Conclusion

5.1 Summary

This thesis presents a study of the role of the interference stabilization effect in the autoionization of the Fano resonance at 17.33 eV in N_2.
The analysis of previous experimental and theoretical works suggested the presence of rotationally-induced symmetry-breaking couplings in gas phase N_2, allowing for the interaction of the $3d\pi_g$ and $4's'\sigma_g$ Rydberg states during autoionization through continuum of different symmetry. Previous ab-initio calculations, which did not include any interaction to a common continuum, were not able to reproduce experimental data on the absorption spectrum of N_2 in the energy range close to the above mentioned Fano resonance.
In order to explain the process from the point of view of the interference stabilization effect it was thus necessary to include in the existing theoretical framework the realistic case of two discrete states coupled to a number of continua with varying strength.
This was accomplished by solving the time-dependent Schrödinger equation for a system composed of a ground state coupled by a short XUV pulse to the continua and the two states. By adiabatically removing the continuum, we obtained a set of coupled differential equations describing the discrete states' amplitudes. Analytical expressions for the quasi-energies of the eigenstates of the Hamiltonian describing the discrete-continuum interaction were found and new cases for interference stabilization were shown to exist; namely, the partially balanced and unbalanced cases.
Furthermore we showed how the new cases of the effect map onto the field-free states time-dependent populations and the photoelectron and absorption spectrum, as these are observables which can be directly compared to experiments.
Finally, by using parameters extracted from previous theoretical works and including the effect of interference stabilization induced by rotational couplings, we were able to fit the experimental XUV absorption profile of the Fano resonance at 17.33 eV in N_2, resolving the existing theoretical and experimental discrepancies and verifying our initial hypothesis.

5.2 Outlook

Due to its very general requirements, the interference stabilization effect should play an important role in a variety of different quantum systems.
In this thesis specifically, I have shown how the effect determines the complex line profile in the autoionization process of N_2 when two resonances with overlapping widths interact with one or more common continua. It is reasonable to expect that this should occur for other members of the same Rydberg series as well. On the other hand, recent transient absorption experiments seem to hint at the presence of interference stabilization in autoionization of other diatomic molecules like O_2 [17]: one of the next steps will be therefore to apply the theory presented here to other molecular and atomic targets.
Furthermore, the theory can be extended to the most general configuration of n discrete states coupled to N continua: although numerical solutions would be necessary, the qualitative knowledge of the effect coming from the two-state case could help disentangle complex multi-electronic dynamics. One could for example devise a pump-probe photoelectron experiment where a band of autoionizing states could be excited by a pump pulse and later probed via probe-induced ionization.
Finally, interference stabilization can also be seen as a two-photon Raman-like transition as the role of the two autoionizing states could be taken by two discrete states below the ionization threshold coupled by an external laser field to the continuum: from this point of view, it shares strong similarities with the famous Stimulated Raman Adiabatic Passage (STIRAP) process [43]. First discovered in 1989 by Bergmann et al. [44], STIRAP is a standard technique used in quantum control and quantum information to transfer population efficiently from an initial to a target state; interference stabilization could hence be used to achieve the same transfer via a continuum. As noise and decoherence still dominate the quantum computing landscape, the way out could be to increase abruptly the coupling to the environment rather than the opposite.

Appendix A

Interference Stabilization and STIRAP

Stimulated Raman Adiabatic Passage (STIRAP)

Stimulated Raman Adiabatic Passage (STIRAP) is an efficient scheme to achieve selective population transfer between an initial and a target state of an atomic or molecular system via an intermediate state. The technique was first developed in 1989 by K. Bergmann et al. [44] and has since been extensively used to optimally control well-defined quantum states using laser light.
Let us hereby describe the simplest STIRAP configuration, as depicted in figure {A.1}. The system is composed of three discrete states $|\Psi(t)\rangle = \sum_i c_i(t)\,|\Psi_i\rangle$ and is interacting with a two-color field $\epsilon_s(\omega_s, t) + \epsilon_p(\omega_p, t)$. The indexes s and p refer respectively to the Stokes pulse, which couples the initial state $|\Psi_1\rangle$ to the intermediary one $|\Psi_2\rangle$, and the Pump pulse, coupling $|\Psi_2\rangle$ and the target state $|\Psi_3\rangle$. The intermediary state $|\Psi_2\rangle$ can also decay radiatively to lower-lying states as depicted in figure. Let us simplify the picture by supposing that the detunings are small, i.e. $\Delta_{p,s} \ll \Omega_{p,s}$.

In order to describe the interaction of the field with the system, we have to solve the time-dependent Schröodinger equation

$$\mathrm{i}\frac{d}{dt}\mathbf{C}(t) = \mathrm{H}(t)\mathbf{C}(t) \tag{A.1}$$

where $\mathbf{C}(t) = [c_1(t), c_2(t), c_3(t)]^{\mathrm{T}}$ is a vector whose elements are the probability amplitudes of the respective bound states and $\mathrm{H}(t)$ is the Hamiltonian. In the Rotating Wave Approximation, the Hamiltonian in atomic units can be written as

$$\mathrm{H}(t) = \begin{bmatrix} 0 & \frac{1}{2}\Omega_p(t) & 0 \\ \frac{1}{2}\Omega_p(t) & \Delta_p & \frac{1}{2}\Omega_s(t) \\ 0 & \frac{1}{2}\Omega_s(t) & \Delta_p - \Delta_s \end{bmatrix} \tag{A.2}$$

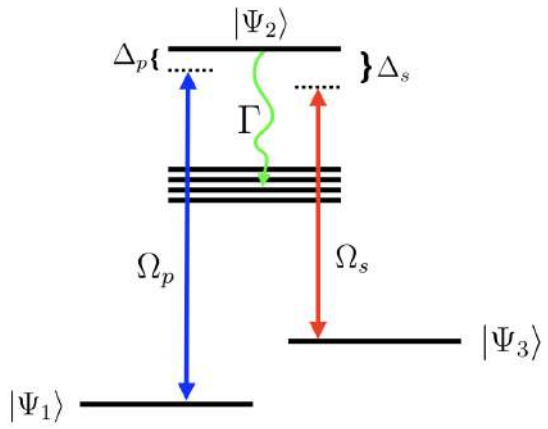

Figure A.1: Three state STIRAP.

where $\Omega_p(t) = d_{2,3} \cdot \epsilon_p(\omega_p, t)$ and $\Omega_s(t) = d_{1,2} \cdot \epsilon_s(\omega_s, t)$ are the Rabi frequencies of the Pump and Stokes pulses. If the one-photon detunings are the same, i.e. $\Delta_p = \Delta_s = \Delta$, the Hamiltonian admits three adiabatic eigenstates:

$$|\Psi_+(t)\rangle = \sin\theta(t)\sin\phi(t)\,|\Psi_1\rangle + \cos\phi(t)\,|\Psi_2\rangle + \cos\theta(t)\sin\phi(t)\,|\Psi_3\rangle \tag{A.3}$$

$$|\Psi_0(t)\rangle = \cos\theta(t)\,|\Psi_1\rangle - \sin\theta(t)\,|\Psi_3\rangle \tag{A.4}$$

$$|\Psi_-(t)\rangle = \sin\theta(t)\cos\phi(t)\,|\Psi_1\rangle - \sin\phi(t)\,|\Psi_2\rangle + \cos\theta(t)\cos\phi(t)\,|\Psi_3\rangle \tag{A.5}$$

where $\theta(t) = \arctan\left(\frac{\Omega_p(t)}{\Omega_s(t)}\right)$ and $\phi(t) = \frac{1}{2}\arctan\left(\frac{\sqrt{\Omega_p^2(t)+\Omega_s^2(t)}}{\Delta}\right)$ are the so-called mixing angles. The corresponding energies of the dressed states are

$$\gamma_\pm(t) = \frac{1}{2}\left(\Delta \pm \sqrt{\Delta^2 + \Omega_p^2(t) + \Omega_s^2(t)}\right) \tag{A.6}$$

$$\gamma_0(t) = 0 \tag{A.7}$$

It is obvious that the dressed state $|\Psi_0(t)\rangle$, coherent superposition of the initial and target state, is a *dark* state, as it has no projections on the intermediate state $|\Psi_2\rangle$ and cannot therefore decay radiatively through Γ. A very efficient population transfer can be achieved precisely due to the presence of this trapped state, which depends only on the mixing angle $\theta(t)$ and therefore on the instantaneous ratio of the Rabi frequencies of the Pump and Stokes fields. Consequently, if one applies the pulses in a *counterintuitive* order, that is

$$\frac{\Omega_p(t)}{\Omega_s(t)} \to 0 \qquad \text{for } t \to -\infty \tag{A.8}$$

$$\frac{\Omega_p(t)}{\Omega_s(t)} \to \infty \qquad \text{for } t \to +\infty \tag{A.9}$$

the mixing angle $\theta(t)$ will evolve from 0 to $\pi/2$, while the dressed state $\Psi_0(t)$ will accordingly evolve from the field-free initial state $|\Psi_1\rangle$ to the target one $|\Psi_3\rangle$. To achieve complete population transfer without losses is therefore fundamental to force the system to remain at all times in the dark state. This can be done by providing an adiabatic evolution in time, that is, the pulses must have a large area, or equivalently

$$\sqrt{\Omega_p^2 + \Omega_s^2} \gg T^{-1} \tag{A.10}$$

where T is the pulse width. Hence, if the adiabatic condition is provided, once we apply a counterintuitive sequence of pulses we will always achieve complete population transfer from the initial state $|\Psi_1\rangle$ to the target one $|\Psi_3\rangle$. In figure {A.2}, we report the sequence of pulses together with the evolution in time of the quasi-energies and bare states' populations for the three-state STIRAP configuration.

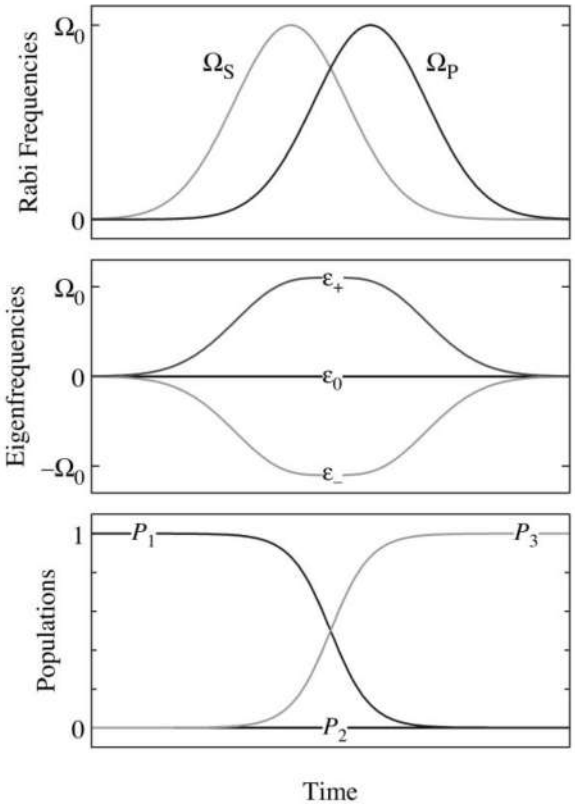

Figure A.2: Time dependence of the Pump and Stokes Rabi frequencies (top panel), of the eigenergies (middle panel) and of the bare states' populations (bottom panel) for a counter-intuitively ordered pulse sequences. Figure adapted from [45].

This scheme can be easily extended to more complex configurations, such as four-state STIRAP or STIRAP chains. We refer the reader to the literature for further details [43, 45].

Interference stabilization and STIRAP

As previously mentioned in this thesis work, interference stabilization can be seen as a two-photon Raman transition between two closely lying states via a continuum. The link between the latter and the Stimulated Raman Adiabatic Passage is therefore clear, as it is enough to substitute the intermediate discrete state of STIRAP with a continuum in our equations to obtain the interference stabilization case. Accordingly, the dark state of STIRAP is substituted in interference stabilization by the quasi-dark state with corresponding quasi-energy (cfr. equation [3.21]):

$$\gamma_+(t) = \frac{1}{2}(E_1 + E_2 - \mathrm{i}\Gamma(t) + \sqrt{\alpha(t)^2 - \Gamma(t)^2}) \tag{A.11}$$

where we introduced a time-dependence in the rates $\Gamma_i(t)$ and $\alpha(t) = \Delta_E + \mathrm{i}(\Gamma_p(t) - \Gamma_s(t))$. The subscripts $_{p,s}$ refer to the Pump and Stokes pulse as in panels **b,c** of figure A.3. It is clear that in the limiting case of very strong coupling, i.e. $\Gamma(t) \gg |E_1 - E_2|$, the losses of the quasi-dark state are minimized, effectively enhancing the efficiency of the population transfer process through the dressed state. Equivalently, in the case of degenerate initial and target state, interference stabilization of two states coupled through a continuum reproduces the limiting case of the simple three-level STIRAP configuration.
In panel **a** of figure A.3, I report the trajectory of the two state system on the quasi-energy surface of the quasi-dark state $|+\rangle$. The surface is defined as the absolute value of the imaginary part of the quasi-energy, i.e. its dissipative part, plotted against the intensity of the Stokes and Pump pulse. The black dots correspond to the trajectory, that is the instantaneous values of the quasi-energy during the dynamics, referring to the counter-intuitive sequence of pulses in panel **b**. To minimize losses, one would have to force the evolution as much as possible on the lower values of the surface which correspond to small dissipation and loss of population. This qualitative picture provides a simple map on which one can follow the dynamics of the STIRAP process through the continuum. Note that the presence of the branching point correspond to the initial point of a sharp edge dividing the map in two sectors of lower and higher dissipation.

Experimental realization of STIRAP through continuum

The very stringent conditions one has to provide to achieve efficient population transfer through the continuum include strong coupling that varies slowly in time, as the adiabatic condition is to be met in order to maintain the system in the quasi-dark state. At the same time, high laser intensities will induce substantial shifts of the energy levels, effectively making it harder to meet the adiabatic condition at all times. The forced evolution of the system through the dark state is therefore harder to achieve in

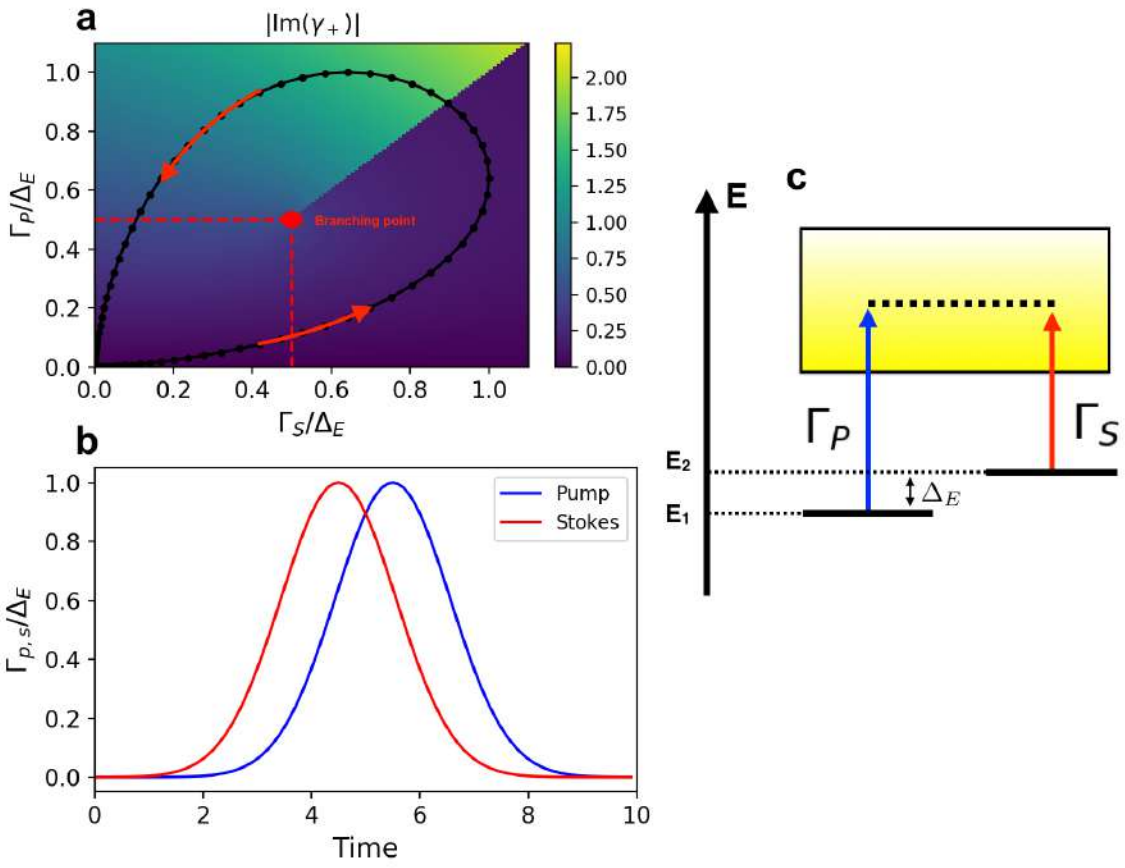

*Figure A.3: Panel **a)**: the trajectory (black dots) of the system on the quasi-energy map, defined as $|Im(\gamma_+)|$, as a function of time. The red arrows represent the direction of the trajectory. Panel **b)**: the Pump and Stokes pulses as a function of time. Panel **c)**: diagram of the STIRAP through continuum system.*

interference stabilization in comparison with STIRAP.
Nonetheless, the first experimental demonstration of population transfer through the continuum was reported in 2005 by Halfmann et al. [46, 47]. In this experiment, the researchers were able to show a population transfer in He from the metastable state $2s^1S_0$ to the excited state $4s^1S_0$ through the ionization continuum of the parent ion. The experiment showed a 29% transfer efficiency, a remarkable result which shows the possibility of transferring a substantial portion of electronic population through the ionization continuum in atomic systems.

Bibliography

[1] F. Krausz and M. Ivanov, "Attosecond physics," *Rev. Mod. Phys.*, vol. 81, no. 163, 2009.

[2] U. Fano, "Effects of configuration interaction on intensities and phase shifts," *Phys. Rev.*, vol. 124, pp. 1866–1878, 1961.

[3] U. Fano, "Sullo spettro di assorbimento dei gas nobili presso il limite dello spettro d'arco," *Il Nuovo Cimento*, vol. 12, no. 3, pp. 154–161, 1935.

[4] M. F. Limonov, M. V. Rybin, A. N. Poddubny, and Y. S. Kivshar, "Fano resonances in photonics," *Nat. Phot.*, vol. 11, 2017.

[5] M. Eckstein, C.-H. Yang, F. Frassetto, L. Poletto, G. Sansone, M. J. J. Vrakking, and O. Kornilov, "Direct imaging of transient fano resonances in n_2 using time-, energy- and angular-resolved photoelectron spectroscopy," *Phys. Rev. Lett.*, vol. 116, no. 163003, 2016.

[6] M. Eckstein, N. Mayer, C.-H. Yang, G. Sansone, M. J. J. Vrakking, M. Ivanov, and O. Kornilov, "Interference stabilization of autoionizing states in molecular N_2 studied by time-, energy- and angular-resolved photoelectron spectroscopy," *Faraday Discuss.*, 2016.

[7] M. V. Fedorov, "Atomic and free electrons in a strong light field," 1998.

[8] M. Fedorov and A. Kazakov, "Resonances and saturation in multiphoton bound-free transitions," *Prog. Quant. Electr.*, vol. 13, pp. 1–106, 1989.

[9] M. V. Fedorov and A. Movsesian *J. Phys. B: At., Mol. Opt. Phys.*, vol. 21, pp. 1133–1134, 1988.

[10] A. M. Popov, O. V. Tikhonova, and E. A. Volkova, "Strong-field atomic stabilization: numerical simulation and analytical modelling," *J. Phys. B: At., Mol. Opt. Phys.*, vol. 36, pp. 126–163, 2003.

[11] Y. I. Heller and A. K. Popov, "Laser-induced narrowing of autoionizing resonances studied by the method of parametric generation," *Phys. Lett.*, vol. 56A, no. 6, pp. 453–454, 1976.

[12] C. Ott, A. Kaldun, P. Raith, K. Meyer, M. Laux, J. Evers, C. H. Keitel, C. H. Greene, and T. Pfeifer, "Lorentz meets Fano in spectral line shapes: A universal phase and its laser control," *Science*, vol. 340, 2013.

[13] M. Raoult, H. L. Rouzo, G. Raseev, and H. Lefebvre-Brion, "Ab initio approach to the multichannel quantum defect calculation of the electronic autoionisation in the hopfield series of n_2," *J. Phys. B: At., Mol. Opt. Phys.*, vol. 16, pp. 4601–4617, 1983.

[14] P. Morin, M. Y. Adam, I. Nenner, J. Delwiche, M. Hubin-Franskin, and P. Lablanquie, "Measurements of partial and differential photoionization cross sections of helium and diatomic molecules in the 15–100 ev range by angular electron spectroscopy," *Nuclear Instr. and Meth. In Phys. Res.*, vol. 208, pp. 761–766, 1983.

[15] W. Demtroder, *Molecular Physics*. Wiley, 2005.

[16] H. Wang, M. Chini, S. Chen, C.-H. Zhang, F. He, Y. Cheng, Y. Wu, U. Thumm, and Z. Chang, "Attosecond time-resolved autoionization of argon," *Phys. Rev. Lett.*, vol. 105, no. 143002, 2010.

[17] C.-T. Liao, X. Li, D. J. Haxton, T. N. Rescigno, R. R. Lucchese, C. W. McCurdy, and A. Sandhu, "Probing autoionizing states of molecular oxygen with xuv transient absorption: Electronic-symmetry-dependent line shapes and laser-induced modifications," *Phys. Rev. A*, vol. 95, no. 043427, 2017.

[18] M. Born and R. Oppenheimer, "Zur quantentheorie der molekeln," *Annalen der Physik*, no. 20, 1927.

[19] PubChem, "Nitrogen."

[20] F. R. Gilmore, "Potential energy curves for n_2, no, o_2 and corresponding ions," *Journal of Quantitative Spectroscopy and Radiative Transfer*, vol. 5, no. 2, 1965.

[21] M. Eckstein, C.-H. Yang, M. Kubin, F. Frassetto, L. Poletto, H.-H. Ritze, M. J. J. Vrakking, and O. Kornilov, "Dynamics of n_2 dissociation upon inner-valence ionization by wavelength-selected xuv pulses," *J. Phys. Chem. Lett.*, vol. 6, pp. 419–425, 2015.

[22] M. Eckstein, *Investigation of Ultrafast Electronic and Nuclear Dynamics in Molecular Nitrogen using an XUV Time Delay Compensating Monochromator*. PhD thesis, Freie Universitat Berlin, 2015.

[23] P. W. Langhoff, S. R. Langhoff, T. N. Rescigno, J. Schirmer, L. S. Cederbaum, W. Domcke, and W. V. Niessen, "Theoretical studies of inner-valence-shell photoionization cross sections in n_2 and co," *Chem. Phys.*, vol. 58, no. 1, 1981.

[24] I. V. Hertel and C.-P. Schulz, *Atome, Molekule Und Optische Physik 2 Molekule Und Photonen-Spektroskopie Und Streuphysik*. Springer-Verlag, 2011.

[25] J. J. Hopfield, "Absorption and emission spectra in the region λ 600-1100," *Phys. Rev.*, vol. 35, no. 1133, 1930.

[26] P. Croteau, J. B. Randazzo, O. Kostko, M. Ahmed, M.-C. Liang, Y. L. Yung, and K. A. Boering, "Measurements of isotope effects in the photoionization of n_2 and implications for titan's atmosphere," *The Astrophysical Journal Letters*, vol. 728, 2011.

[27] K. P. Huber, G. Stark, and K. Ito, "Rotational structure in the hopfield series of n_2," *J. Chem. Phys.*, vol. 98, no. 6, 1993.

[28] A. Stolow, A. E. Bragg, and D. M. Neumark, "Femtosecond time-resolved photoelectron spectroscopy," *Chem. Rev.*, vol. 104, pp. 1719–1757, 2004.

[29] M. Wu, S. Chen, S. Camp, K. J. Schaffer, and M. B. Gaarde, "Theory of strong-field attosecond transient absorption," *J. Phys. B: At., Mol. Opt. Phys.*, vol. 49, 2016.

[30] M. Hentschel, R. Kienberger, C. Spielmann, G. Reider, N. Milosevic, T. Brabec, P. Corkum, U. Heinzmann, M. Drescher, and F. Krausz, "Attosecond metrology," *Nature*, vol. 414, pp. 509–513, 2001.

[31] A. Einstein, "On a heuristic point of view concerning the production and transformation of light," *Annalen der Physik*, vol. 17, pp. 132–148, 1905.

[32] A. T. J. B. Eppink and D. H. Parker, "Velocity map imaging of ions and electrons using electrostatic lenses: Application in photoelectron and photofragment ion imaging of molecular oxygen," *Rev. Sci. Instr.*, vol. 68, no. 3477, 1997.

[33] A. Wituschek, *Velocity Map Imaging*. Albert-Ludwigs-Universitat Freiburg, 2016.

[34] M. Eckstein, J. Hummert, M. Kubin, C.-H. Yang, F. Frassetto, L. Poletto, M. J. J. Vrakking, and O. Kornilov, "Alignment and characterization of the two-stage time delay compensating xuv monochromator," *arXiv*, no. 1604.02650, 2016.

[35] V. Dribinski, A. Ossadtchi, V. A. Mandelshtam, and H. Reisler, "Reconstruction of abel-transformable images: The gaussian basis-set expansion abel transform method," *Rev. Sci. Instr.*, vol. 73, no. 2634, 2002.

[36] G. H. Golub and C. Reinsch, "Singular value decomposition and least squares solutions," *Numerische Mathematik*, vol. 14, no. 5, 1970.

[37] S. Feneuille, S. Liberman, E. Luc-Koenig, J. Pinard, and A. Taleb, "Field-induced stabilisation of Stark states in the rubidium atom," *J. Phys. B: At., Mol. Opt. Phys.*, vol. 15, pp. 1205–1216, 1982.

[38] J. Liu, P. McNicholl, D. Harmin, J. Ivri, T. Bergeman, and H. Metcalf, "Interference narrowing at crossings of sodium Stark resonances," *Phys. Rev. Lett.*, vol. 55, no. 2, pp. 189–192, 1985.

[39] P. Knight, M. Lauder, and B. Dalton, "Laser-induced continuum structure," *Phys. Rep.*, vol. 190, no. 1, pp. 1–61, 1990.

[40] P. Dirac, "The quantum theory of emission and absorption of radiation," *Proc. R. Soc. Lond. A*, vol. 114, no. 767, pp. 243–265, 1927.

[41] E. Fermi, *Nuclear Physics*. University of Chicago Press, 1950.

[42] W. Leonski, R. Tanas, and S. Kielich, "Laser-induced autoionization from a double fano system," *J. Opt. Soc. Am. B*, vol. 4, no. 1, 1987.

[43] K. Bergmann, N. V. Vitanov, and B. Shore, "Perspective: Stimulated raman adiabatic passage: The status after 25 years," *J. Chem. Phys.*, vol. 142, no. 170901, 2015.

[44] U. Gaubatz, P. Rudecki, S. Schiemann, and K. Bergmann, "Population transfer between molecular vibrational levels by stimulated raman scattering with partially overlapping laser fields. a new concept and experimental results," *J. Chem. Phys.*, vol. 92, pp. 5363–5376, 1990.

[45] N. V. Vitanov, T. Halfmann, B. Shore, and K. Bergmann, "Laser-induced population transfer by adiabatic passage techniques," *Annu. Rev. Phys. Chem.*, vol. 52, pp. 763–809, 2001.

[46] T. Peters, L. P. Yatsenko, and T. Halfmann, "Experimental demonstration of selective coherent population transfer via a continuum," *Phys. Rev. Lett.*, vol. 95, no. 103601, 2005.

[47] T. Peters and T. Halfmann, "Stimulated raman adibatic passage via the ionization continuum in helium: Experiment and theory," *Optics Communications*, vol. 271, pp. 475–486, 2007.

Statement of authorship

I hereby declare that this M. Sc. thesis has been composed by myself, and describes my own work, unless otherwise acknowledged in the text. All references and verbatim extracts have been quoted, and all sources of information have been acknowledged. It has been accepted in any previous application for a degree.

Nicola Mayer,
Berlin, October 24th, 2017